Distinct heterochromatin-like domains promote transcriptional memory and silence parasitic genetic elements in bacteria

Haley Minami Amemiya[1,2,5],Thomas J. Goss[3], Taylor M. Nye[4], Rebecca Hurto[3], Lyle A. Simmons[4], and Peter L. Freddolino[1,2,3,*]

1: Cellular and Molecular Biology Program, University of Michigan Medical School, Ann Arbor, MI, USA
2: Department of Computational Medicine and Bioinformatics, University of Michigan Medical School, Ann Arbor, MI, USA
3: Department of Biological Chemistry, University of Michigan Medical School, Ann Arbor, MI, USA
4: Department of Molecular, Cellular, and Developmental Biology, University of Michigan, Ann Arbor, MI, USA
5: Current Address: Broad Institute of MIT and Harvard
*: Correspondence to: petefred@umich.edu

Keywords: Nucleoid-associated proteins / Chromatin / Gene regulation / Bacterial gene regulation

Abstract

There is increasing evidence that prokaryotes maintain chromosome structure, which in turn impacts gene expression. We recently characterized densely occupied, multi-kilobase regions in

the *E. coli* genome that are transcriptionally silent, similar to eukaryotic heterochromatin. These extended protein occupancy domains (EPODs), span genomic regions containing genes encoding metabolic pathways as well as parasitic elements such as prophages. Here, we investigate the contributions of nucleoid-associated proteins (NAPs) to structuring of these domains, by examining the impacts of deleting NAPs on EPODs genome-wide in *E. coli* and *B. subtilis*. We identify key NAPs contributing to the silencing of specific EPODs, whose deletion opens a chromosomal region for RNA polymerase binding at genes contained within that region. We show that changes in *E. coli* EPODs facilitate an extra layer of transcriptional regulation, which prepares cells for exposure to exotic carbon sources. Furthermore, we distinguish novel xenogeneic silencing roles for the NAPs Fis and Hfq, which are essential for cell viability in the presence of domesticated prophages. Our findings reveal previously unrecognized mechanisms through which genomic architecture primes bacteria for changing metabolic environments, and silences harmful genomic elements.

Introduction

All organisms must organize immense amounts of genetic information into a relatively small physical space within the cell. Paradoxically, the maintenance and accessibility of the DNA architecture is required for efficient DNA replication, repair, and transcription, and thus for proper cell division required to sustain life. In the bacterium *Escherichia coli* (*E. coli*), chromosome structure is mediated by roughly a dozen small, basic nucleoid-associated proteins (NAPs) [1–3] that work in concert to modulate supercoiling, DNA looping, and distant chromosomal contacts [4–8]. Despite substantial research effort, it is largely unclear how individual NAPs impact the overall structure of the chromosome, due in part to their promiscuous and overlapping binding across the genome [3,9,10].

In order to gain a comprehensive understanding of the contribution of NAPs to global protein occupancy and gene expression, we used *in vivo* protein occupancy display at high resolution (IPOD-HR). IPOD-HR is a method that provides a global snapshot of areas in the genome where proteins are bound to DNA, thus yielding insight into genome-wide regulation and

structure [11,12]. IPOD-HR revealed approximately two hundred regions of the *E. coli* genome that are densely packed with protein but exclude RNA polymerase, inviting striking comparisons to heterochromatin found in eukaryotes [13]. These regions are referred to as extended protein occupancy domains (EPODs), and identified based on the presence of high levels of protein occupancy over a length of 1 kb or more [11]. While EPODs have been shown to be partially occupied by NAPs and in some cases overlap with known binding sites for NAPs such as H-NS [12], the contributions of individual NAPs on EPOD formation remains unexplored. Our previous findings, consistent with studies in the literature, have implicated H-NS as a dominant gene silencer in *E. coli* [1,5,12,14]. H-NS has the capacity to form filaments, tightly compacting dsDNA. *In vitro*, it has been shown that the two types of filaments, linear or bridged, block transcription initiation, while only bridged filaments block transcription via blocking elongation [15–17] . Other proteins, such as Hha and the H-NS paralog StpA, promote the formation of H-NS filaments and modulate their structural properties [6,18]. In addition to H-NS's role in global gene silencing, it is well documented to specifically silence horizontally acquired DNA [12,19–22]. While the dominant form of filaments *in vivo* remains unknown, it is clear that H-NS plays a major role in transcriptional silencing in the bacteria that carry it.

Recent data suggests that EPODs contribute to both the regulation of metabolic pathways and the silencing of horizontally acquired DNA [12,23], however the NAPs mediating this response for individual EPODs are unknown. Additionally, evidence suggests that bacterial genomes have integration hotspots for horizontally acquired DNA [24]. We have found that EPODs have a higher Tn5 integration frequency compared to the rest of the genome [12], perhaps giving insight that EPODs may be functional units that serve as hotspots for foreign DNA integration. Additional data using different mechanisms of horizontal gene transfer would be required to further investigate the extent to which EPODs show enhanced integration rates, as opposed to simply forming on horizontally acquired DNA once it has already integrated. Understanding the key protein components of EPODs and EPODs' roles in genome organization will shed light on the relationship between the regulation of transcription and genome architecture in bacterial genomes.

Here, we investigate the contributions of the major NAPs in *E. coli* to maintaining the pattern of global protein occupancy, and the effects of that occupancy on gene expression. Rather than simply observing where one particular protein binds, we monitor the complete set of changes in protein occupancy caused by loss of any single NAP. We show that loss of any single NAP

results in changes to the global landscape of protein occupancy, albeit often less dramatic than might be expected, as we show that NAPs are able to compensate for each other to maintain EPOD structure even after single NAP knockouts. Further, we demonstrate the function of NAP mediated silencing of rare carbon metabolism and suggest that this mechanism facilitates a transcriptional memory response. Additionally, we describe a previously unidentified prophage silencing role for NAPs Hfq and Fis. Finally, we demonstrate the presence of EPOD-like structures in the evolutionary distinct Gram-positive *Bacillus subtilis*, which function similarly to facilitate silencing of metabolic pathways and horizontally acquired genes.

Results

Large-scale patterns of protein occupancy are highly maintained across conditions and laboratory isolates

In order to investigate the contributions of the major *E. coli* nucleoid-associated proteins to the genome-wide pattern of protein occupancy, we applied our recently developed IPOD-HR method [13] to profile the changes in global protein occupancy on the chromosome in the presence of several deletions of nucleoid-associated protein coding genes. The IPOD-HR procedure begins similarly to a chromatin immunoprecipitation (ChIP) experiment, in which cells are crosslinked under a physiological condition of interest, lysed, and the DNA digested (**Appendix Figure S1A**). However, rather than pull down a single protein target with an antibody as in ChIP, a phenol-chloroform extraction is performed wherein an enrichment of protein-DNA complexes forms in a white disc at the aqueous-organic interphase (**Appendix Fig. S1A**). The disc is isolated and washed thoroughly, and then DNA purified from the disc and compared to an input sample to reveal the locations on the genome that were bound by proteins at the time of crosslinking. The raw IPOD-HR signal contains contributions both from RNA polymerase and from regulatory proteins. In order to visualize protein bound to DNA aside from RNA polymerase, we perform an RNA polymerase ChIP-seq experiment in parallel and subtract the binding of RNA polymerase from our raw IPOD-HR signal (**Appendix Fig. S1B**). In-depth methodological details are given in the Methods section and in [13]. In our initial applications of IPOD-HR in *E. coli*, we found that the method was able to reveal the dynamics of individual transcription factor binding sites after both genetic and physiological perturbations [13]. We saw

in contrast, however, that hundreds of regions of extended protein occupancy (termed **E**xtended **P**rotein **O**ccupancy **D**omains or EPODs [11]) were fairly static across all tested conditions (three transcription factor deletions and three growth conditions) [13]. Given that EPODs appear to arise largely due to the binding of nucleoid associated proteins (NAPs), in the present work, we examined the contributions of different NAPs proteins to the pattern of EPODs along the chromosome.

To identify condition-dependent EPOD locations in the *E. coli* genome we applied EPOD calling equivalent to that in [12]. There are two EPOD thresholds defined by regions that are greater than 1,000 bp in length over which the rolling mean protein occupancy in that region exceeds a specified percentile compared to the rest of the genome (see Materials and Methods). We term the two levels of stringency used here as “Loose EPODs” (75th percentile cutoff; the “relaxed” threshold) and “Strict EPODs” (90th percentile cutoff) **(Fig. 1A;** further explained in [11]**)**. Here, we will focus primarily on “Strict EPODs” unless otherwise noted. It was previously shown that the ~200 EPODs identified across the *E. coli* MG1655 (WT) genome show significantly enriched overlaps with loci encoding genes involved in metabolism and silencing of mobile elements [12]. As remodeling of nucleoid organization has been previously detected in response to environmental changes, such as media richness and growth phase [25–27], we tested whether EPODs were one of the functional units that mediated changes across growth conditions. To examine the robustness of these domains under various physiological conditions, we performed IPOD-HR on an MG1655 isolate (referred to as “WT”), varying the media type and growth phase. IPOD-HR was performed as previously described [12]; samples were taken at mid-exponential growth phase or deep stationary growth phase (D.S.; described in Materials and Methods below), in both rich defined media and minimal media with glucose (see Materials and Methods). For all experiments, we used defined media to maintain consistency in physiological experiments with buffer conditions, salts, etc and to avoid the noted variation occurring in Lysogeny Broth (LB medium) [28,29]. Even within *E. coli* MG1655 isolates, there are genetic differences from variation in parental origin [30] that have led to differences in what is deemed “WT” across different laboratories. To examine the robustness of EPODs between relatively similar isolates with minor genetic differences, we utilized another MG1655 isolate (labeled WT (2)). In comparison to WT, WT (2) is *crl*$^{+}$*, gatC*$^{+}$*, glpR*$^{+}$*,* contains point mutations in *ybhJ* and *mntP*, and has an intact *dgcJ* (see Methods for details). The variations between different MG1655 isolates are an important consideration when comparing across various MG1655 datasets, as our data suggests that small genetic differences may lead to wider changes in

gene regulation and protein occupancy landscapes compared to changes in media sources, as we will discuss in detail below.

The number and overall genomic coverage EPODs across conditions and genetic backgrounds remained relatively stable (**Fig. 1B,C**), with the greatest increases in coverage and counts in cells in deep stationary phase and the WT (2) isolate. To examine the changes in the locations and boundaries of EPODs, we calculated a measure that we refer to as the symmetrized overlap distance, given by the difference between unity and the geometric mean of the EPOD overlaps:

$$1 - \sqrt{A_B \times B_A}$$

Where A_B is the fraction of condition B's EPODs overlapped by the relaxed threshold EPODs ("Loose EPODs"; example in **Fig. 1A**) contained in condition A, and B_A is the fraction of condition A EPODs overlapped by the loose threshold EPODs from condition B. A value of 0 indicates identical EPOD locations, since both overlaps would be 1. The use of loose EPODs in the comparisons as opposed to strict avoids overstating the differences between conditions based on minor thresholding differences, and emphasizes large and systematic changes in occupancy. The symmetrized overlap distances between all pairs of conditions examined here are shown in **Figure 1D**. Values within the heatmap displayed are calculated using the fraction of EPODs contained in the relaxed threshold EPODs, defined as in [12], for each condition. Hierarchical clustering analysis of these distances reveal that the major differences stem decreasingly from growth phase, genotype, and then media changes (**Fig. 1D**). Notably, the EPOD location profiles for the two MG1655 isolates considered here were more similar to each other than the WT deep stationary phase condition, but in all cases a substantial majority of EPODs are conserved across conditions. These findings support ongoing research that shows major changes in nucleoid composition during later phases of growth [8,9]. Previous investigation of EPODs under baseline growth conditions (exponential growth in rich defined media) demonstrated that genes contained in EPODs were enriched for several functionalities, including DNA transposition, cytolysis, and LPS biosynthesis [12]. To identify the pathways maintained across all conditions considered in **Figure 1**, we ran iPAGE [31] to associate which gene ontology (GO) terms fell within EPODs relative to the rest of the genome ("Background"). We found that three GO terms remained highly enriched in EPODs under all four conditions shown here: cytolysis, LPS biosynthetic pathway, and cellular response to acid chemical, demonstrating that EPOD-mediated regulation of these functionalities persists across both physiological condition and the selected cell lineages (**Appendix Fig. S2**).

Important genetic differences have previously been observed between various MG1655 isolates, which include mutations expected to have regulatory consequences [30]. In the case of the WT vs WT (2) MG1655 isolates considered here, one of the main genetic differences is the presence of an IS1 insertion sequence in the *dgcJ* gene (a putative diguanylate cyclase) in WT that is absent in WT (2). Cyclic di-GMP generally regulates the switch between adhesion/biofilm formation and motility across a range of bacteria [32]. A *dgcJ* mutant exhibits increased motility [33]. In addition, WT (2) contains an intact *crl* allele compared with the IS5-disrupted allele present in WT, and the Crl regulon likewise contains a multitude of genes involved in motility and adhesion [34]. Based on these important genetic differences, we expected that the overall regulatory states of WT and WT (2) would substantially differ with regards to motility and biofilm formation, although the direction of the effect is impossible to predict *a priori* due to the lack of information on the precise effect of the *dgcJ* IS1 insertion (which could in principle cause gain or loss of function) and the complicated interaction of various GGDEF proteins in regulating motility and biofilm formation [33]. Indeed, we observed an enrichment of EPODs on biofilm and adhesion related genes in the WT (2)-specific EPODs (**Appendix Figure S2**), indicating that the additional EPODs unique to WT (2) were enriched on operons involved in establishing a sessile lifestyle. As noted above, the strains considered here also differ in genotype at *gatC, glpR, ybhJ*, and *mntP*; although it appears unlikely based on the genes involved, we cannot rule out contributions from the differences at those loci in the observed changes in EPOD locations. Taken together with our deep stationary phase results, we show that IPOD-HR is able to detect changes in global protein occupancy due to genetic and environmental differences. We also note that while most EPODs are preserved across a range of conditions, the positions of some EPODs do indeed change in response to genetic and/or environmental perturbations.

Silencing of the non-functional LPS gene pathway is maintained across conditions

To better understand the dynamics of protein occupancy across different conditions at a locus that shows a heavily maintained EPOD, we examined the changes in occupancy at a representative region, the LPS biosynthesis locus (the *waa* operon) across conditions (**Fig. 1E**). The LPS pathway was noted to be silenced by EPODs in our initial findings [12]. Typically, *E. coli* express these operons as part of O antigen biosynthesis, a highly beneficial cellular component that increases resistance to phage infection and environmental pressures [35–40]. However, MG1655 contains an insertion element in *wbbL*, an upstream component of the LPS

pathway, rendering *wbbL* non-functional [41]. Consistent with prior observations, we observe robust protein occupancy and minimal RNA polymerase occupancy across all conditions (**Fig. 1E**), although a qualitative change in the locations of the high-occupancy regions is apparent in deep stationary phase, perhaps reflecting a turnover in the predominant NAPs present under that condition. Without functional genes in this pathway, there are no biological benefits to expressing downstream genes under various physiological conditions. We speculate that these components of the LPS pathway are silenced due to the insertion element in *wbbL* as a method to conserve resources. While the exact mechanism for the establishment and maintenance of *waa* operon silencing is currently unknown, we hypothesize that silencing may have been selected for over the course of the subsequent evolution of MG1655.

Nucleoid associated proteins are the main components of EPODs

We hypothesized that the maintenance of EPODs was largely driven by the NAP occupancy. H-NS has been widely described as a major component of the *E. coli* nucleoid in exponential growth, specifically inhibiting transcription and silencing mobile elements and prophages [6,14,19]. We compared published H-NS binding sites within EPODs compared to background (*i.e.*, the remainder of the genome) and found significant enrichments of H-NS binding in EPODs across all considered conditions (**Fig. 1F**), consistent with previous observations [11]. Thus, H-NS is facilitating silencing of regions across the genome robustly in varying media, growth phase, and slight genotype differences. However, we also found previously that while the majority of EPODs overlap with known H-NS binding regions, a substantial fraction do not [12]. In addition, the fact that H-NS is present at a particular EPOD does not necessarily mean that it is the only factor (or even a necessary or sufficient factor) in forming that EPOD and silencing the genes there. We thus sought to assess whether other NAPs facilitate silencing of specific EPODs or if H-NS is the major silencing factor of EPODs across the *E. coli* genome.

The binding locations and biological roles of nucleoid associated proteins (NAPs) have been difficult to define largely because of their promiscuous binding across the genome [10]. Due to their propensity to bind DNA and their high abundance in the cell, we hypothesized that multiple NAPs contribute to EPODs. To examine the contributions of a range of *E. coli* NAPs to EPODs, we made single deletions of the most abundant *E. coli* NAPs (*hns*, *stpA*, *fis*, *hfq*, *ihfAB*, *dps*, and *hupAB*) and performed IPOD-HR on the deletion strains. Since StpA is a known paralog of H-NS and forms bridged filaments across DNA [6,7], we also created an *hns/stpA* double knock-

out and performed IPOD-HR. As the NAP Dps is primarily expressed during stationary phase of growth [42,43], we performed additional IPOD-HR experiments on WT and *Δdps* cells that were collected during the deep stationary phase stage of growth (defined in Materials and Methods). EPOD counts and coverage slightly varied across genotypes tested (**Fig. 2A,B**), with the largest loss of coverage observed in *ΔstpAΔhns*. To examine shifts in EPOD locations, we again measured the symmetrized overlap distance (defined for **Fig. 1D**) and performed hierarchical clustering (**Fig. 2C**). The greatest changes in EPOD locations relative to the baseline condition (WT cells in exponential phase) occur within *ΔstpAΔhns* and *Δihf,* both of which cause profound changes in the profile of EPOD locations. The deep stationary phase samples cluster together, indicating similar shifts in EPOD locations. Interestingly, *Δhns* and *Δhfq* cluster together, perhaps suggesting a similar role in silencing at some EPODs. Several other NAP deletions show minimal effects on EPODs relative to WT cells, including deletions of *hupAB*, *stpA*, and *dps* (in exponential phase), indicating that at least under baseline conditions, these proteins do not contribute strongly to defining EPODs.

Different EPODs are comprised of distinct combinations of NAPs

To identify the relative contribution of different NAPs in maintaining a 'standard' set of EPODs present in WT cells during exponential phase growth, we calculated the average of the total protein occupancy signal across every EPOD location and other genomic regions for each genotype (**Fig. 2D**). When comparing the WT median (pink dashed line) vs. the deletion mutant medians (blue), NAPs contributing to protein occupancy at EPODs that are normally present during exponential growth phase display a statistically significant dip in occupancy. Consistent with our prior observations, the loss of occupancy at normal EPOD boundaries in *ΔstpAΔhns* cells is particularly profound. However, the *hns* single mutant shows only a minor loss of occupancy which indicates that StpA can largely compensate for its loss. Several other NAP deletions also showed significant drops in occupancy at the standard EPOD locations, often with a heavy lower tailed or even bimodal distribution of occupancy changes suggesting that only some subset of EPODs were affected in each case. At the same time, in many cases, RNA polymerase occupancy at a subset of affected EPODs is observed to rise (**Fig. EV1A**), indicating a derepression of some EPODs upon deletion of *hupAB*, *hfq*, *hns*, *ihf*, or (especially)

in the *stpA/hns* double knockout. The impact of the double (*stpA* and *hns*) deletion is also demonstrated when looking at the association between a previously published H-NS ChIP-seq dataset [17] with EPODs in each mutant, where we see that EPODs present in the double mutant lack H-NS enrichment compared to background (**Appendix Fig. S3**). Inspection of the patterns of both total protein occupancy and RNA polymerase occupancy across the *waa* operon provides an instructive example. Whereas single deletions of *hns* or *stpA* show a minor effect on the integrity of the *waa* EPOD, the *ΔstpAΔhns* cells show nearly complete loss of occupancy in this region (**Fig. 2E**). At the same time, there is a concomitant gain in RNA polymerase occupancy and induction of RNA expression of *waa* operon genes (**Fig. 2F,G**), demonstrating that H-NS and StpA act jointly to maintain silencing of the *waa* operon. While either can compensate for the other, the loss of both silencers leads to substantial de-repression of genes in this region.

Additionally, all NAPs exhibited changes in EPOD locations that impacted the overlap of called EPOD regions. We examined the fraction of EPODs contained in the relaxed threshold EPODs, and found the overlap between EPOD locations among different genotypes dipped as low as 40% (**Fig. EV1B**). Changes in protein occupancy compared to WT at all regions of the genome and downstream hierarchical clustering suggests a similar role of Hfq and H-NS in silencing specific regions of the genome (**Appendix Fig. S4**).

HMM categorization reveals distinct EPOD classes dictated by individual NAP profiles

Our data thus permit us to identify which NAPs regulate specific EPODs across the genome. To provide an automated high-level classification of the regions across the genome specific to particular NAPs, we used our IPOD-HR occupancy and RNA polymerase ChIP-seq datasets across the NAP deletions and trained a six-state Hidden Markov Model (HMM) that split the genome up into six classes (see Materials and Methods for details). We were able to identify three classes (2, 3, and 5) that were associated with EPODs, which exhibited significant enrichments of IHF motifs [44], Hfq binding (See note in Materials and Methods), H-NS binding [20], and Fis binding [20], as well as a low abundance of motifs for the known DNA methylases - Dam and Dcm [44] (**Table 1**). In particular, HMM class 2 is especially strongly associated with H-NS binding and likely represents H-NS/StpA dependent EPODs (with IHF also apparently

contributing). HMM class 5 is associated with high levels of Hfq and Fis binding and may represent EPODs comprised in part by these two factors. In addition, class 5 had a high abundance of transcription factor binding sites and promoters [44], further implicating this class serving a regulatory role. HMM class 3 represents yet another category of EPODs that at present cannot be assigned. The utility of the HMM classification is apparent in providing a quick interpretation of the differences between EPODs. For example, the *waa* operon is almost entirely associated with HMM class 2 (**Fig. 2E**), which we assign as an H-NS filament. On the other hand, the borders of the EPOD instead fall into HMM class 3 or 5 and show loss of occupancy in an *hns* deletion strain even if *stpA* is intact (**Fig. 2E**), whereas the class 2 region does not. Thus, we find that StpA and H-NS together contribute to large protein regions across the genome, and are the main components silencing the LPS biosynthesis pathway. At the same time, we observe the presence of two distinct classes of EPOD occupancy (class 3 and class 5) that appear largely H-NS independent, and likely represent different types of large-scale repressive protein occupancy.

It is essential to note that the HMM classes themselves are built solely off of changes in total protein occupancy and RNA polymerase occupancy in the presence of various NAP deletions. Thus these data cannot by themselves distinguish between direct binding of the indicated NAPs, vs. indirect effects on protein occupancy occurring downstream of the NAP deletions. However, the enrichment and depletion statistics shown in **Table 1** reflect direct measurements of the binding profiles of the indicated factors, and thus provide strong independent evidence for enrichments of binding of specific NAPs at the indicated HMM classes (*i.e.*, H-NS at classes 2 and 3, IHF and Hfq at classes 2 and 5, Fis at class 5).

Metabolic pressures induce changes in EPODs

Many EPODs overlap operons involved in metabolic pathways, and thus silence pathways that may not be actively used in the cell under the conditions that we studied. For example, during growth in glucose rich defined media we observed an EPOD, associated with HMM class 2 (H-NS filament), overlapping the *idnDOTR* operon, specifically in the promoter of the operon. The *idn* operon is essential for the metabolism of carbon sources such as idonate and 5-keto gluconate, which are not present under typical laboratory conditions. In particular the *idnD* gene codes for the enzyme L-idonate 5-dehydrogenase, which catalyzes the oxidation of L-idonate to 5-ketogluconate [45–47]. The *idnDOTR* operon and *idnK* are known to be transcriptionally

regulated by CRP, IdnR, GlaR, and GntR, but, to our knowledge no connection to regulation by NAP occupancy has been described [48]. Upstream of the *idnDOTR* operon, there is a 215-bp regulatory region that lies in between *idnK* and *idnD* [45]. In this region, there is a single putative IdnR/GntR binding site, CRP binding site, and an UP element [45]. Bausch ***et al.*** previously showed that induction of this pathway can occur due to exposure to L-idonate or 5-keto-gluconate (5KDG) [45]. The local positive regulator, IdnR, is activated by 5KDG [47], and promotes the induction of the rest of the operon. Following exposure to 5KDG in the absence of glucose, IdnT enables uptake of the carbon source, IdnD (as previously mentioned) catalyzes the reversible reduction of L-idonate to 5-ketogluconate, IdnO catalyzes the oxidation of 5-ketogluconate to D-gluconate, and idnK catalyzes the phosphorylation of D-gluconate which then proceeds through the Entner-Doudoroff pathway to be metabolized [47]. Since the *idn* operon appears to be controlled by three local and one global regulators, the question arises of what additional regulatory role might be provided by the apparent silencing EPOD covering the *idn* promoter under standard defined media conditions used here.

To explore the mechanisms of silencing at the *idnDOTR* operon, we first referred to our NAP deletion dataset to see whether specific NAP(s) silenced the operon. Data from a previous H-NS ChIP-seq dataset [20] plus the classification of this region as a type 2 EPOD in our HMM suggested the presence of H-NS bound to the *idn* promoter region. We performed RNA-seq in the *ΔstpAΔhns* background compared with the parental cells, and discovered that H-NS and StpA indeed repress expression of the *idnDOTR* operon (**Fig. EV2A,B**). We leveraged this knowledge to address whether we could induce changes in protein occupancy at the EPOD covering the *idn* promoter by performing a carbon source shift experiment outlined in (**Fig. 3A**; further explanation in Materials and Methods). Briefly, cells were grown in minimal media with 0.2% glucose, shifted to minimal media with 0.2% 5-keto-D-gluconate (5KDG) as a sole carbon source, and shifted back to minimal media with 0.2% glucose as the carbon source. In all conditions, cells were collected at an OD_{600} of ~0.1 for both IPOD-HR to examine changes in EPODs and RNA-seq for changes in expression. Notably, there was a severe lag for growth in 5KDG. We found that growth in 5KDG led to a reduction in protein occupancy and loss of the EPOD within the *idnDOTR* operon promoter (**Fig. 3B; raw data represented in Fig. EV2B**). Upon shifting the cells back to glucose, both the original pattern of protein occupancy and the EPOD were restored (**Fig. 3B**). The consistency with the previously reported H-NS binding [20], coupled with our own findings that protein occupancy is reduced while there is an induction of

idnDOTR operon genes in the *stpA* and *hns* double mutant (**Fig. EV2B**), further supports our hypothesis that H-NS is a major contributor to the suppression of the *idnDOTR* operon (**Fig. 3B**). The loss of EPOD occupancy in the 5KDG condition was accompanied by an induction of expression of the *idnDOTR* operon, and repression when EPOD occupancy was restored upon the return to glucose as a carbon source (**Fig. 3C**). Due to the long lag in growth during the transfer from glucose to 5KDG as a carbon source, we examined the correlation between the expression of all genes in the three conditions to see whether there were broad changes in expression when cells were forced to metabolize an exotic carbon source (**Fig. 3D**, top panel). The Spearman correlation was extremely high when comparing all conditions ($\geq$0.9), suggesting that changes are localized to the *idn* operon and the small set of other genes specifically regulated in response to the 5KDG carbon source. Similarly, the symmetrized overlap distances comparing the variation in EPOD locations across conditions were low, again supporting the notion that changes are specific to the induced operon (**Fig. 3D**, bottom panel) and that no global rearrangement of protein occupancy occurs during growth on 5KDG.

Given the sophisticated regulatory logic implemented at the *idn* promoter by a combination of local (GlaR, GntR, IdnR) and global (CRP) regulators, it is unclear what additional function is played by the apparently repressive EPOD covering this region. Drawing inspiration from the behavior of chromatin modifications in eukaryotes (e.g. [49–52]), we hypothesized that one function of EPODs could be to facilitate transcriptional memory. We thus performed head-to-head competition experiments in KDG-containing and glucose-containing media comparing the growth of cells that have been exposed to KDG (**Fig. 4A**). We utilized MG1655 *lacZ* cells and a reference strain MG1655 *lacZ::cat* in order to enable colony counting on MacConkey-lactose plates as a read out for the competitions. WT (MG1655 *lacZ*) cells were exposed to M9 minimal media + KDG for 48 hrs, back diluted and grown in M9 minimal media + glucose. During these growth periods, WT cells and *lacZ::cat* cells that had been grown in + glucose overnight were back diluted and mixed together into a tube containing KDG or Glucose as carbon sources. Serial dilutions were plated onto MacConkey-lactose plates immediately after mixing and after 48 hrs of growth for each carbon source condition (**Fig. 4A**).

As shown in **Figure 4B**, we found that immediately after growth in KDG media, the KDG-exposed cells showed strongly increased fitness during competition in KDG relative to the KDG-naive cells (Day 0). The advantage of the KDG-exposed cells was lessened, but still significant, after 12 hours of outgrowth in glucose minimal media (Day 0.5), and then strongly diminished by

24 hours (Day 1) and subsequently absent. We interpret the very strong initial competitive advantage of cells taken immediately from KDG as reflecting a cellular state directly adapted to growth in KDG (including accumulations of the IdnO/IdnT proteins), whereas the persistent advantage of the previously KDG-exposed cells after outgrowth in glucose demonstrates a memory effect where the cells more readily respond to the presence of KDG as a sole carbon source upon repeated exposure despite the transcriptional regulatory state having reset to be virtually indistinguishable from the original round of growth in glucose minimal media prior to the second 5KDG challenge (**Fig. 3**). Given the long outgrowth between the 0 day and 0.5 day 5KDG challenges (the KDG-exposed cells used in the competitions underwent no fewer than 8.0 doublings in M9 Glu between the 0 day and 0.5 day timepoints (count data are given in **Appendix Table S1**), it is expected that essentially all of the Idn proteins would have been diluted to irrelevant levels. While additional direct evidence is needed, our findings are consistent with the possibility that the structure of the EPOD in this region is such that transcriptional initiation is faster upon second induction within some time window after an initial induction, providing a transcriptional memory that facilitates responses to repeated stresses. Given that EPOD occupancy on the *idn* promoter re-forms rapidly after transfer back to M9 Glu media (Fig. 3), any 'memory' must be implemented by molecular information beyond the simple presence or absence of protein binding. This response may be mediated by formation of bridged vs. unbridged H-NS filaments in this region, by post-translational modification of H-NS comprising the EPOD (analogous to the histone code [53]), or binding of unknown accessory factors. Further investigation of the kinetics of EPOD re-formation after induction is lifted, and indeed the identities of proteins that bind to the *idn* region immediately after EPOD re-formation, will be required to distinguish between the possible mechanisms noted above.

We also note that the competitive fitness in glucose of cells immediately after KDG exposure was particularly poor, and indeed, in a separate set of monoculture experiments, we observed that the lag time for cells transferred from stationary phase in 5KDG media to glucose media was significantly longer than for the transfer from glucose media to glucose media (**Fig. 4C**; note that the pregrowth procedures and growth conditions differ between the competition experiments and the monocultures in **Fig. 4C**, likely accounting for the even more pronounced post-KDG lag observed in the latter case). One possible explanation for these findings would be that some of the gene products induced to metabolize 5KDG may themselves be detrimental under normal growth conditions, and thus another role of the EPOD at the *idn* promoter may be to ensure tight silencing of these genes until they are needed. It is also possible, however, that

some other aspect of global physiological state (e.g., stress-induced changes in transcription or translation), rather than *idn* gene expression, are responsible for the observed lag.

Multiple NAPs contribute to the silencing of prophages

In addition to metabolic processes, we also found that genes within EPODs were overrepresented in Gene Ontology (GO) terms associated with annotated prophages [12]. Across the *E. coli* genome, there are a number of xenogeneic elements that have been integrated and can be potentially toxic to the cell, although maintenance of these elements can also be beneficial, as they can promote resistance in the face of antibiotics [54]. H-NS is known to silence cryptic prophages, and is likely to contribute to silencing the majority of horizontally acquired DNA in *E. coli* [54,55]. IPOD-HR successfully resolved known H-NS silenced prophages (**Fig. 5A**), where reductions in protein occupancy and corresponding increases in accessibility to RNA polymerase are observed in an *hns* knockout strain. For example, we observed a decrease in protein occupancy along the promoter and gene body regions of *sieB*, a gene in the Rac prophage that controls phage superinfection [56], and corresponding increases in RNA polymerase occupancy, in the *hns* knockout strain. This indicates that while EPOD binding isn't completely absent in the *hns* mutant across this particular prophage, there is still a quantitative reduction in silencing protein occupancy and corresponding transcriptional de-repression. As noted above, not all EPODs correspond to H-NS binding; therefore it is likely that not all silenced prophages are located in H-NS repressed regions. To examine the role of other nucleoid associated proteins in silencing prophages, we calculated the mean protein occupancy across WT EPODs that overlap prophages, and determined how those occupancies changed upon deletion of different NAPs. Overall median decreases in occupancy across prophage-containing EPODs are observed upon deletion of *dps, hupAB, hfq, stpA, hns, stpa/hns, ihf,* and in both deep stationary phase samples compared to WT (occupancy distributions and statistical significance calling are shown in **Fig. 5B).** In addition, as shown in **Fig. EV3**, many individual EPODs show substantial changes in occupancy even in cases where the median of the distribution is unchanged.

Inspired by our findings above that only the combined deletion of *hns* and *stpA* can reveal large changes in occupancy of many H-NS silenced EPODs (**Fig. 2E-G**), the minor loss of occupancy in some genetic backgrounds led us to investigate whether there are certain NAPs that work together to silence specific toxic elements. We examined the change in occupancy from each

condition vs WT at WT EPODs that overlap prophages and performed hierarchical clustering analysis (**Fig. 5C**) to identify regulators that play similar roles. Interestingly, *Δhns* and *Δhfq* are clustered together, as are *ΔstpA* and *Δfis,* suggesting prophages are silenced by multiple factors and NAPs. The association of multiple NAPs to specific prophage EPODs may indicate that they act cooperatively, for instance in the case of H-NS and StpA, or independently, which in many cases remains to be determined. Our findings implicate the well documented RNA chaperone Hfq [57,58] (which has also been shown to compact dsDNA [59,60]) as a novel silencer of prophages at the level of protein occupancy across large genomic regions. Since H-NS and StpA are paralogs that bind to similar regions of the chromosome, we speculated that Hfq and Fis might play similarly complementary roles to each other in terms of silencing some prophages despite their lack of structural similarity. In addition, from our HMM analysis, both Fis and Hfq binding are enriched in HMM class 5 (**Table 1**), again suggesting a link between the silencing roles and binding locations of Fis and Hfq.

Fis and Hfq are required for cell viability in a prophage dependent manner

Building off of the noted co-occurrence of Fis and Hfq binding in HMM class 5 EPODs, we screened the genome for EPODs that contained prophages that lost global protein occupancy upon deletion of *fis* or *hfq* individually (e.g., **Fig. 6A**). RNA-seq analysis revealed that the genes within the prophage region depicted in **Figure 6A** were de-repressed in both a *Δhfq* and *Δfis* background, despite only minimal losses in total protein occupancy (**Fig. 6B**). While Fis and Hfq are both NAPs, highly expressed, and bind promiscuously across the genome, they are not known to silence genes via the formation of densely occupied large-scale binding regions. Fis, while known more in the literature as a transcriptional activator [61,62], can inhibit transcription and act as a repressor in certain contexts [63,64]. Hfq is well known as a RNA chaperone [65] and can bind nucleic acids (including DNA) across the faces of the wheel-like homohexamer [59]. Therefore, we were not surprised to find that comparing the log fold-change of expression (relative to WT) of *Δhfq* and *Δfis* cells were not highly correlated among all genes (**Fig. 6C**). However, when examining only prophage genes, most genes were induced in one or both of the knockout genotypes (**Fig. 6D**). We quantified the number of genes that were up or down in each genotype or both using the quadrant map in **Figure 6E**. We applied this map and counted the rate ratios comparing all genes vs prophage genes in each quadrant. The rate ratios of all

genes vs prophage genes in the quadrant which represented induced expression in both *Δhfq* and *Δfis* was significantly higher in prophage genes (**Fig. 6F**). Thus, prophage genes are specifically and significantly enriched among the set of genomic loci that are repressed by both Fis and Hfq, suggesting that Fis and Hfq bind and silence similar prophages, and also that a substantial fraction of all prophages in fact appear to have strongly Fis/Hfq dependent occupancy.

Since the expression of genes from lysogenized bacteriophages can be toxic to the cell even if they are no longer able to form replication-competent virions (particularly if a lytic operon is induced), we asked whether the combined loss of *hfq* and *fis* would more strongly impact cell physiology. We performed P1 transduction experiments in a WT, MG1655 background and a *Δfis* background, where we attempted to delete the genomic copy of *hfq*. Interestingly, there was a dramatic loss of transduction efficiency in the *Δfis* background, and we were not able to create the *Δhfq Δfis* mutant (**Fig 6G**). The transduction efficiency for *hfq::kan* dropped more than 100-fold in the *Δfis* background, and the very small number transductants that did form colonies could not be propagated upon restreaking. To test whether the deletion of *fis* impacts transduction efficiency as a whole, we attempted the same experiment deleting *cspE*, another gene that has not been associated with prophage silencing, and did not observe a similarly dramatic loss in transductants, with simple loss of *fis* leading to only a ~4-fold loss in transduction efficiency; thus, we infer that loss of *hfq* and *fis* is synthetic lethal. To further test our hypothesis of synthetic lethality between *fis* and *hfq*, we attempted to complement the combined loss of *fis* and *hfq* using a copy of *hfq* on a temperature sensitive plasmid. We thus cloned *hfq* and its native promoters on a plasmid with a temperature sensitive origin of replication [66]. The plasmid was placed into WT and *Δfis* cells, and the genomic copy of *hfq* was deleted using P1 *vir* transduction (see Materials and Methods). Cells were grown at permissive temperature (30° C), and spot titers were performed on LB and LB + chloramphenicol plates to measure CFUs of the culture and presence of the plasmid. Cultures were then shifted to 42° C, which prevents plasmid replication, and thus induces dropping of the plasmid containing *hfq*. After 8hrs of growth at 42° C, spot titers were performed to assess CFUs. We found again that the combination of *Δhfq Δfis* was not viable (**Fig. EV4**), supporting

our conclusion of synthetic lethality. We hypothesized that the expression of prophages silenced by Fis and Hfq led to the inviability phenotype. To test this hypothesis, we utilized the strain MDS42 [67] , which lacks the mobile elements and prophages in the *E. coli* K12 genome. We placed the temperature sensitive plasmid containing *hfq* in MDS42 and MDS42 *Δfis* cells and performed the same temperature shift experiment as described above. Removal of the prophages from the genome, restored viability (**Fig. EV4**). We also observed a substantial rescue of transduction efficiency, which reached the same level in the *Δfis* background as that of the control transduction with *cspE::kan* (**Fig. 6G**); thus, the lethality of the *Δhfq Δfis* is dependent on the presence of at least one of the regions lost in MDS42. Since 42 large regions are deleted from MDS42, we asked if we could identify specific prophage regions that led to inviability. Since there is loss in occupancy in both *Δhfq* and *Δfis* in the **Figure 6A** region (R1:564815-585633, within the DLP12 prophage; **Table 2**), we deleted only R1:564815-585633, and found a partial rescue of transduction efficiency (**Fig. 6G**). We found another region that met the same criteria (R3, within the Qin prophage; **Table 2**), and also saw rescuing effects (**Fig. 6G**). Another region that contained prophages, but did not dip in occupancy in both genotypes, did not impact viability (R2, within the Rac prophage; **Table 2**; **Fig. 6G**). Thus, we were able to define regions that contribute to viability, and hone in on specific prophages that are silenced by Fis and Hfq and, in the absence of repression by those two NAPs, prevent cell growth. In particular, loss of either of two prophages (DLP12 or Qin) was sufficient to restore the viability of a *Δhfq Δfis* double mutant. This novel interaction defines a new role for NAPs in regulating the expression of prophages, implicating additional *E. coli* NAPs in the establishment of defense mechanisms against horizontally acquired DNA. It is especially notable that the NAPs apparently involved in this case are not the classic xenogeneic silencers (H-NS/StpA), but rather, appear to represent a separate and complementary system for silencing potential lethal prophage gene expression.

Extended protein occupancy domains silence horizontally acquired DNA across diverse species

Because it relies only on elementary physico-chemical principles rather than specific affinity reagents, IPOD-HR is an approach that could be implemented in a wide variety of bacterial

species. To further our understanding of conserved features that regulate bacterial genome architecture, we investigated whether a distantly related bacterial species contained EPODs. We performed IPOD-HR on the Gram-positive Firmicute *Bacillus subtilis (B. subtilis)* -- a soil dwelling bacterium that has the ability to enter a number of developmental platforms upon nutrient deprivation or other environmental stressors, including the formation of desiccation resistant endospores, biofilm formation, genetic competence, and swimming/swarming motility phenotypes [68]. We performed IPOD-HR in *B. subtilis* strain PY79 and found multi-kb regions of protein occupancy (EPODs) spanning genes that function in a number of metabolic pathways, suggesting a feature conserved with *E. coli* (**Fig. 7A**). Many of these pathways are activated in times of nutrient limitation and stress, similarly to the silenced pathways we observe in *E. coli*. As regions of protein occupancy were observed in horizontally acquired DNA in *E. coli,* we proposed that regions of protein occupancy may play a role in horizontally acquired DNA in *B.subtilis.* As *B. subtilis* is naturally competent, the tight regulation of competence development is especially important to regulate and protect against the acquisition of harmful exogenous DNA elements. Surprisingly, we found that many large negative occupancy peaks overlapped annotated prophage genes (**Fig. 7B**), appearing similar to EPODs but inverted in sign.

One of the main regulators of competence in *B. subtilis* is Rok, which acts as a direct repressor of competency genes, regulates several secreted proteins, and is involved in repression of mobile genetic elements [68–70]. Due to the impact of Rok on gene regulation, coupled with the promiscuous binding activity to A+T-rich DNA, we propose that Rok may be a main component of protein occupancy in *B. subtilis.* Surprisingly, while we did not see an enrichment of Rok binding in EPODs using available *rok-myc* ChIP-chip data [70], Rok binding was highly correlated with the negative occupancy regions (**Fig. 7C,D**). To investigate this further, we performed IPOD-HR in *⊿rok* cells and found that indeed, the loss of Rok resulted in an increase in RNA polymerase binding at sites correlated with Rok binding, and loss of negative occupancy regions found in the WT condition (**Fig. 7C**). We examined whether negative peaks were associated with discrepancies with read mapping efficiency and found that there were no changes in the distribution of reads in background, EPODs, or negative peaks (**Fig. EV5A**). We subsequently performed our analysis pipeline to incorporate negative occupancy and found that these negative EPODs, termed nEPODs, correlated with Rok binding and were enriched for genes known to be regulated by Rok, such as sporulation genes and genes involved in

competence activation. Importantly, we did not observe correlations with any suspected nucleoid associated proteins or global regulators in negative peaks in *E. coli*, where instead negative peaks are associated with highly transcribed genes (**Fig. EV5**). Thus, whereas in *B. subtilis* regions of extended negative IPOD signal appear indicative of gene silencing due to Rok binding, large regions of negative measured IPOD occupancy in *E. coli* are areas of active transcription. These assessments are critical when understanding global protein occupancy in new species. The most likely explanation for our observations is that Rok-DNA complexes are likely depleted rather than enriched from the interphase during the IPOD-HR phenol chloroform extraction, which would give rise to a large region of apparent depletion in the resulting signal. It is possible that other proteins will be encountered in other species that have similar properties, although as noted above, we found no evidence for such behavior among *E. coli* proteins.

Positive (standard) EPODs were also apparent in the *B. subtilis* data, and we found them to be highly correlated with SMC binding (**Fig. 7E,F**), which is known to compact the genome in preparation for chromosomal segregation [71–73]. Our findings align with known datasets [74], and further our understanding of the role of nucleoid binding proteins in defining the genome landscape across species. Without the dependency on antibody-based methods, we can explore unknown protein functions across a variety of developmental platforms and species. These findings highlight the broad utility of IPOD-HR, with the ability to detect both conserved and novel genome architecture features in a variety of distantly related bacterial species. In addition, we see that the general pattern of large regions of high protein occupancy apparently silencing genes horizontally acquired DNA is an extremely widespread feature, occurring in at least two bacterial species separated by more than 2 billion years of evolution.

Discussion

There is increasing evidence of a regulated genome architecture in *E. coli*, both in terms of its three dimensional structure [26,75–77] and in terms of the landscape of protein occupancy on the genome. Both of these classes of features are largely supported by binding of NAPs [12]. IPOD-HR enabled us to study global changes in chromosomal architecture - here defined as highly protein occupied regions of the genome - across species and implicated NAPs as the main component of EPODs. Here, we show the robustness of these large protein domains

across media conditions, growth phase, and small genotype differences (**Fig. 1**). The maintenance of EPODs across conditions and ancestral strains aligns with the idea that EPODs serve an important regulatory silencing role. A variety of questions emerge: How are EPODs maintained through replication and growth? What recruits proteins to these regions? Further studies are being performed to examine the role of methylation in maintenance and recruitment of protein to EPOD regions. As horizontally acquired DNA and methylation have been shown to be intertwined in *E. coli* [78], and we found that *dam* and *dcm* sites are depleted in EPODs, we suspect that DNA methylation may play a role in regulation of EPODs containing prophages.

Our study shows that EPODs are partly composed by NAPs in *E. coli* (**Fig. 2**), with the largest contribution clearly made by the major transcriptional silencers H-NS and StpA, but other pairs of NAPs making important contributions at a subset of loci. Due to the wide binding capacity of NAPs across the genome, the question regarding recruitment to EPODs emerges again. IPOD-HR successfully shows losses in occupancy upon deletion of NAPs, however, there may be accessory proteins that facilitate recruitment and maintenance. IPOD-HR may miss subtle changes in proteins that are not as abundant in the cell, so we have begun to design proteomic analysis of EPODs to define the exact composition of EPODs.

We were able to define the key proteins involved in EPOD regulation of metabolic pathways (**Fig. 3,4**) and silencing of prophages across the genome (**Fig. 5,6**). EPODs appear to mediate the formation of transcriptional memory (**Fig. 4**), which allows for strong repression of a rarely-used metabolic operon when it has not been transcribed in recent memory, but aids in faster induction of genes important for metabolic response after a single exposure to a relevant nutrient. This type of regulation poses exciting ideas for understanding how architectural proteins facilitate a genome architecture regulation across the genome. Importantly, understanding bacterial genome regulation can be incredibly useful for biotechnology purposes, especially in the case where cells can be grown in a number of conditions that may induce changes in their overall genome architecture that can impact induction of particular genes.

We have also identified a novel silencing mechanism for prophages and toxic elements across the genome. Together, Hfq and Fis are required to silence some prophages, most notably DLP12 (contained in R1 of **Fig. 6**) and Qin (R3 of **Fig. 6**) prophages. What defines particular prophages to recruit Hfq and Fis remains to be explored. However, these findings contribute to an overarching theme of the genome structure serving as an immune response to a variety of

horizontally acquired DNA. As we have previously shown, reporter constructs integrate with higher frequency in EPODs and are efficiently silenced [12,23]. We propose that EPODs serve as DNA sinks for foreign DNA, and quickly silence potentially harmful elements. Further investigation into the mechanisms underlying this response will bolster our view of the defenses of bacterial species against potentially harmful genetic elements.

Many NAPs and their functions are conserved across bacterial species, and the overall roles of NAPs in establishing large regions of silencing protein occupancy appear to be conserved even beyond the reach of recognizable homologs of any given NAP. We found that the use of genome architecture as a mode of immunity may also be conserved in a distantly related species to *E. coli*, *B. subtilis* (**Fig. 7**). The exploitation of such a system has a number of promising outcomes. For instance, work established here could inform new antibiotic approaches for pathogenic bacteria by targeting proteins required to suppress toxic elements already in existence in the genome. In addition, understanding how bacteria recruit and build their genome architecture around foreign DNA can inform on how bacteria interact with their environment. The manipulation of this process may allow us to utilize bacteria in innovative ways, such as novel biosensors or for protein engineering.

Materials and Methods

Strain construction

The MG1655 “WT” isolate used in all figures was obtained from Hani Goodarzi (Tavazoie Lab, then at Princeton University) in 2009, and is isogenic with ATCC 700926, with the exception of an IS1 insertion at position 991 in *dgcJ* [79]. The MDS42 strain was obtained from Alison Hottes in 2009 (Tavazoie Lab, then at Princeton University) and contains a C->T mutation in *ribD* and missing coverage for *lysV[67].* These modifications may be ancestral to MDS42, or specifically present in our MDS42 parental strain. MDS42 deletions were validated using PCR. The MG1655 (2) isolate was obtained from the Jakob Lab at the University of Michigan in 2018. The strain appears to arise from the ATCC 47076 lineage of MG1655 [30], and thus is *crl*$^{+}$, *gatC*$^{+}$, and *glpR*$^{+}$; relative to the reference sequence for this lineage, however, the MG1655(2) strain also contains point mutations in *ybhJ* (L54I) and *mntP* (G25D), with unknown functional implications (genotypes obtained via analysis with breseq [80]). The MG1655 *lacZ::cml-gfp* cells

used as a reference strain in the competition experiments were separately obtained from Hani Goodarzi (Tavazoie Lab, then at Princeton University).

NAP deletion strains:

All nucleoid associated protein (NAP) gene deletions were performed in the same MG1655 "WT" base strain stock discussed above. All NAP deletions were obtained by P1 transduction [80] of the FRT-flanked *kanR* marker from the corresponding knockout strain of the Keio collection[81,82]. With the exception of Δ*ihfA:: Km* Δ*ihfB::Clm*(*ΔihfAB*) and Δ*hupA* Δ*hupB::Km (ΔhupAB),*the pCP20 plasmid [83] containing Flp recombinase was used to excise the *kanR*marker, leaving a small scar in the place of the original open reading frame. Once candidates were isolated for each deletion and contained the pCP20 plasmid, they were grown overnight at 42°C to drop the temperature sensitive pCP20. The overnight cultures were streaked onto LB plates and grown overnight at 37°C. Individual colonies were replica plated onto appropriate selective plates to ensure the loss of both the marker and pCP20 plasmid. The *ΔihfAB* and *ΔhupAB* strains were not cured due to incredibly low efficiency to excise markers via pCP20, and markers were retained to avoid potential suppressor mutations.

Bacillus subtilis strains

The *B. subtilis* PY79 and rok::kan strains came from the Simmons lab at the University of Michigan. Details of the genome sequence can be found in [84] .

Media/culture conditions

LB (Lennox) media (10g/L tryptone, 5g/L yeast extract, 5g/L NaCl) was used for cloning and recovery of cryogenically preserved cells, with addition of 15g/L bacteriological agar for plating.

In the case of physiological experiments, we used appropriately supplemented versions of M9 defined minimal medium (6 g/L Na_2HPO_4, 3 g/L KH_2PO_4, 1 g/L NH_4Cl, 0.5 g/L NaCl, 1 mM $MgSO_4$). Minimal M9 medium (M9/min) contained includes 0.2% (w/v) carbon source (glucose or glutamine or 5-Keto-D-gluconic acid potassium salt), 0.4 mM CaCl2, 40 μM ferric citrate, and the micronutrient mixture typically incorporated in MOPS minimal media[29]. For all of the remaining IPOD-HR experiments, we used our M9 rich defined medium (M9/rdm) incorporated

with 0.4% (w/v) glucose, MOPS micronutrients, 4 μM CaCl2, 40 μM ferric citrate, and 1x supplements ACGU and EZ as used in MOPS rich defined medium [29].

B. subtilis cell growth and harvest for IPOD-HR

For *Bacillus subtilis* strains were struck from frozen stocks and grown on LB plates overnight at 37°C. WT and Δ*rok* strains were inoculated into LB and LB supplemented with 5 μg/mL kanamycin, respectively, from a plate wash at a starting an OD_{600} of 0.025 and grown at 37°C with shaking to an OD_{600} between 0.65 and 0.85. Rifampin was added to a final concentration of 150 μg/mL and cultures were incubated for an additional 10 minutes at 37°C with shaking. Sodium phosphate (final concentration 0.01M) and formaldehyde (1% v/v) were added to 30 mL aliquots of culture and cross-linked at room temperature for 5 minutes with shaking. Reactions were quenched by the addition of 0.333M glycine for 10 minutes at room temperature. Cells were collected via centrifugation and watched twice with ice-cold PBS and cell pellets were subsequently flash frozen in liquid nitrogen and stored at -80°C.

E. coli cell growth and harvest for IPOD-HR

Cryogenically preserved cells were streaked onto an LB plate and grown in the media of interest with $1/10^{th}$ of the carbon source indicated overnight at a temperature of 37°C and shaking at 200 rpm. The culture was back diluted into fresh, prewarmed media to an OD_{600} of 0.003 the next day. The culture was grown to the target OD_{600} (0.2, except in the case of deep stationary phase samples, described below) and treated with a final concentration of 150 μg/mL of rifampicin and incubated for 10 minutes under the same growth conditions previously described. The cultures were rapidly poured into a 50 mL conical tube and mixed with concentrated formaldehyde/sodium phosphate (pH 7.4) buffer sufficient to yield a final concentration of 10 mM NaPO4 and 1% v/v formaldehyde. Crosslinking proceeded for 5 minutes at room temperature and quenched with an excess of glycine (final concentration 0.333 M) for 10 minutes with shaking at room temperature. The crosslinked cells were chilled on ice for 10 min and washed twice with 10mL ice cold phosphate buffered saline (PBS). The resulting pellets were carefully dried, remaining media pipetted and discarded, and snap-frozen in a dry ice-ethanol bath and stored at -80°C for no longer than 1 month.

Deep stationary samples followed the same process of being grown in the appropriate media overnight and back diluted to an OD_{600} 0.003. Once the cells reached an OD_{600} of 0.2, they were grown for an additional 24 hours, treated with rifampicin for 20 min, and proceeded through the same treatment for crosslinking as described above.

Cell lysis and DNA preparation

IPOD-HR interface extraction, RNA polymerase chromatin immunoprecipitation, and crosslinking reversal and recovery of DNA was performed as previously described [12]. Due to the high biomass of deep stationary phase cells, cells were diluted 10x prior to lysis. In the case of the *B. subtilis*, samples were sonicated 4 times for 5s at 25% power with 15s between pulses**.**

Preparation of next-generation sequencing (NGS) libraries

All DNA samples were prepared for Illumina sequencing using the NEBNext Ultra (or Ultra II) Library Prep Kit (NEB product #E7370 or #E7103, respectively). The NEBNext Ultra II Library Prep Kit was used on the *Δhns ΔstpA* and biological replicate 2 of the deep stationary phase samples (*Δdps* and corresponding WT). We consulted with NEB to confirm that there are no differences between the kits that would impact our results. Single index or dual index primers from NEB were used in the prep. The manufacturer's instructions were followed with the same modifications as listed in [12].

All libraries were sequenced on an Illumina NextSeq instrument.

Analysis of NGS data, read quality control and preprocessing, DNA sequencing and protein occupancy calling, and feature calling was performed as previously described [12]. In brief, after removal of technical sequences (adapters) and trimming of low quality read ends, reads were aligned to the U00096.3 reference genome (*E. coli* samples) or py79 reference genome (*B. subtilis* samples) using bowtie2 with "very sensitive, end to end" presets. Read densities were then calculated at 5 bp resolution across the chromosome, and quantile normalized. Overall effects on fragment abundance due to distance from the origin of replication were removed by dividing each dataset by a spline-smoothed version of the corresponding input data, and then the resulting occupancy tracks were rescaled to each have the same mean value. Separate IPOD and RNA polymerase ChIP occupancy tracks were calculated based on the $\log_2$ ratio of

normalized fragment abundances in each pulldown sample and the corresponding input sample, and the RNA polymerase subtracted IPOD-HR signal was then calculated based on a LOESS fit between the observed IPOD and ChIP occupancies (as described in detail in [12]).

Rescaling of IPOD-HR occupancy tracks and subsequent EPOD calling

While we have previously shown the robustness of the IPOD-HR analysis pipelines for both deletions of local regulators and substantial changes in physiological conditions [12], we found that for the nucleoid-associated protein deletions considered here, in many cases the assumptions underlying the IPOD-HR normalization methods (that the overall shape of the distribution of occupancy values across the genome would not change substantively between conditions) was violated. We thus modified the EPOD calling scheme to be able to compare EPOD count, coverage, and occupancy across NAP deletion datasets, where some NAP deletions are sufficient to substantively shift the overall score distribution, due to the large changes in overall protein binding caused by deletion of any one NAP. We rescaled the IPOD-HR occupancy tracks, beginning with the robust z score values indicating occupancy at every five base pairs of the genome, using the following procedure: We found the intersection of EPODs between each NAP deletion and WT with a minimum fractional overlap of 0.2, and plotted the mean occupancy of each overlapped EPOD (NAP deletion vs. WT). We then used a robust linear model with Huber's T for M estimation to estimate the slope of the NAP deletion values as a function of the WT values for the same EPODs, and used the slope to rescale the NAP deletion dataset by dividing the robust z score values by the slope across the genome -- thus, we rescaled the overall protein occupancy in each condition to bring into register the observed occupancies at regions that were highly occupied both in that deletion and in the wild type cells. These new values were used as input to call EPODs using the algorithm described in [13]: we calculated 512 bp and 256 bp rolling means across the genome, and set as a threshold score the 90^{th} percentile (for normal EPODs) or 75^{th} percentile (for loose EPODs) from the 256 bp rolling mean signal. Then,any region of the genome at least 1,024 bp in length with a median occupancy score from the 512-bp smoothed signal above the threshold score was considered a potential EPOD. Potential EPODs were expanded in both directions on the genome as far as possible while maintaining an median occupancy score above the specified threshold, and without ever reaching an occupancy score below zero. To call EPODs in the NAP deletion datasets considered here, we set the cutoff of what would be counted as an EPOD using the WT thresholds and applied this to all datasets (after the rescaling described above). In

summary, these rescaling and thresholding enabled us to make more accurate comparisons between EPODs and occupancy across the NAP deletion datasets. By bringing the observed occupancies at conserved EPODs into register with each other across the different genotypes in our dataset. The procedure described here represents the best normalization across datasets that can be achieved in the absence of a global standard (e.g., a spike-in sample), which would provide a simpler adjustment with fewer assumptions and may be advisable for future work.

5KDG growth experiments

Experimental design for IPOD-HR collection and RNA-seq experiments on KDG exposure (Figure 3):

Cells were grown from a cryogenic stock on LB plates at 37°C, and inoculated into our M9 minimal medium including 0.02% glucose at 37°C. In the morning, cultures were back diluted to an OD_{600} 0.003 in fresh, pre-warmed M9 minimal medium including 0.2% glucose at 37°C. Once cells reached a target OD_{600} 0.2, cells were pelleted and washed twice with 5 mL of warmed PBS. 1 mL of sample was mixed with 1mL DNA / RNA shield and flash frozen in a dry ice-ethanol bath and stored at -80°C. The remainder of the cells were placed in our M9 minimal medium including 0.2% 5-Keto-D-gluconic acid (5-KDG; Sigma Aldrich: Catalog #K4125) to an estimated OD_{600} of 0.1 and placed at 37°C. Cells were grown to an OD ~0.2, and collected for IPOD-HR, 1 mL for RNA-seq, and back diluted to an estimated OD_{600} of 0.003 in M9 minimal medium with 0.02% glucose. Once cells were grown to an OD_{600} ~0.2 in 0.02% glucose, cells were collected for IPOD-HR and 1 mL for RNA-seq.

Experimental design for KDG competition experiments (Figure 4B):

Our competition experiments were conducted in head-to-head mixed growth between a strain of interest and a (typically isogenic) *lacZ::cat* strain. For each competition, the two competing strains were pregrown under appropriate prior conditions (see below), and then 10 microliters of the pregrowth culture for each of the two competing strains were inoculated into prewarmed destination media (separate tubes of M9+glucose and M9+KDG, 2 mL per tube) and allowed to grow for approximately 48 hours at 37° C with shaking at 200 rpm. Both immediately after inoculation, and again after 48 hours, a dilution series of each culture was spotted on MacConkey/lactose plates to enable counting of the lac+ and lac- colonies present.

At the beginning of each experimental series, both the test (*lac*+) and reference (*lac*-) strains were pregrown overnight in M9 + 0.2% glucose (starting from a single colony taken from an LB plate); this is referred to as 'Day -1' in our experimental timelines, and indicates that both the test and reference strains are KDG-naive. At the same time as assembly of the initial competitions, the test strain for each experimental series was then back diluted 200x into 2 mL of M9 + 0.2% KDG, and grown for 48 hours. The KDG-adapted test cells were then competed against a fresh culture of the reference cells that had been grown overnight in M9+glucose -- we refer to this as 'Day 0' in our experimental timelines. At the same time as the Day 0 competition, some of the KDG-adapted test cells were also diluted 200x into fresh M9 + 0.2% glucose and allowed to grow overnight. These glucose-recovered test cells were completed the following day against reference cells that had likewise been grown for 12 hours and 24 hours in M9 + 0.2% glucose, resulting in our 'Day 0.5' and 'Day 1' competitions, respectively (that is, the test cells are 0.5 or 1.0 day removed from their KDG exposure). We continued several additional cycles of passaging the test cells in M9 + 0.2% glucose followed by competition with naive reference cells, resulting in competitions referred to as 'Day 2', 'Day 3', etc. -- in all cases the stated duration is the number of days (and passages in M9 + 0.2% glucose) that the test cells are removed from their growth in KDG.

For each competition, we established competitive indices λ for the test cells relative to reference cells separately in KDG and in glucose media, using the following equation:

$$\lambda_m = log_2\left(\frac{cfu_{test,final} \,/\, cfu_{reference,final}}{cfu_{test,initial} \,/\, cfu_{reference,initial}}\right)$$

Where *m* denotes a media type (either M9+glucose or M9+KDG) and the specified cell counts (cfu) are taken for that media type. A pseudocount of 0.1 was added to all counts, as in a small number of cases zero colonies of one type or the other were observed due to the lopsidedness of the competition. One quantity of particular interest is the difference in the competitive fitness of the test strain (relative to its reference) in KDG vs. that in glucose; thus, we define the difference in fitnesses, Δλ, as

$$\Delta\lambda = \lambda_{KDG} - \lambda_{Glucose}$$

Here, more positive values of Δλ indicate that the test strain is (relative to the reference) more fit during competition in KDG media, after normalization by their competition growth in glucose

media; these values are used for the analysis. The quantity $\Delta\lambda$ is referred to as the "Log2 Fitness Ratio in KDG (relative to naive)" in **Fig. 4B.**

Experimental design for Figure 4C:

Similar to the experiments performed in Fig. 3, cells were grown from a cryogenic stock on LB plates at 37°C, and inoculated into our M9 minimal medium including 0.02% glucose at 37°C. In the morning, cultures were back diluted to an OD_{600} 0.003 in fresh, pre-warmed M9 minimal medium including 0.2% glucose at 37°C in a total volume 150uL with 100uL of mineral oil in a plate reader. Measurements were taken every 10 min at 37C with shaking to calculate lag times. Once cells reached an OD_{600} ~0.2, they were back diluted to an OD_{600} of 0.01 in M9 minimal medium with 0.2% 5KDG. Cells were grown to an OD_{600} ~0.2, then diluted to an OD_{600} 0.003 in M9 minimal medium with 0.2% glucose and grown to an OD_{600} ~0.2.

Growth curves (using $\log_2$-scaled optical densities [ODs]) were smoothed using a cubic spline with one knot per five hours (or fraction thereof) in the data; we then identified the maximum value of the slope of the resulting spline as the growth rate. The lag time was calculated by projecting a line with a slope equal to the growth rate through the point at which the most rapid growth was observed and took the time at which that line intercepted a horizontal line at the initially observed $\log_2$ OD for that culture. Summary statistics were calculated via Bayesian regression as implemented in the brms R package, with population-level effects for the experiment under consideration and default brm values for all other arguments.

RNA isolation and sequencing preparation

All RNA-sequencing samples were collected and prepared for sequencing as follows. Once cells were grown to the appropriate OD_{600}, 2.5mL of culture was mixed with 5mL of RNAprotect (Qiagen: Catalog #76506), vortexed and incubated at room temperature for 5 min. Cells were spun at 4°C for 10 min at 5,000 x *g* in a fixed-angle rotor. The supernatant was removed, and the pellet was flash frozen in a dry ice-ethanol bath and stored at -80°C. For RNA extraction, the pellet was resuspended in 100uL of TE and treated with 177kU (1uL) Ready-lyse lysozyme solution (Lucigen: Catalog #R1804) and 0.2 mg (10uL) proteinase K (Thermo Fisher Scientific: Catalog #EO0492), incubated for 10 min at room temperature with vortexing every 2 min. The RNA was purified using RNA Clean and Concentrator kit-5 (Zymo: Catalog #R1014), treated

with 5 units of Baseline-ZERO DNase (Epicentre: Catalog #DB0715K) in the presence of RNAse inhibitor (NEB: Catalog #M0314L) for 30 min at 37°C. RNA was purified again using RNA Clean and Concentrator kit-5 (Zymo: Catalog #R1014). RNA was flash frozen in a dry ice-ethanol bath and stored at -80°C.

rRNA depletion was performed using the bacterial rRNA depletion kit following manufacturer instructions (New England Biolabs (NEB): Catalog #E7850L). The only modification performed was the last step, where instead of a bead clean up, we used the RNA Clean and Concentrator kit-5 (Zymo: Catalog #R1014).

Sequencing preparation was performed using the NEBNext Ultra Directional RNA Library Prep Kit for Illumina following manufacturer instructions (NEB: Catalog #E7420L) for rRNA depleted RNA. Random primers were used, and RNA was considered intact for the NEBNext Ultra protocol. Slight modifications to the protocol are as follows. To purify cDNA, the Oligo clean & concentrator was used (Zymo: Catalog #D4061). Following adapter ligation, DNA was purified using DNA Clean & Concentrator-5 (Zymo: Catalog #D4014). Dual index primers from NEB were used in the prep. Libraries were sequenced on an Illumina NextSeq.

RNA-seq analysis began with read preprocessing identical to that described in [12], through the end of the bowtie2 alignment stage. After alignment to the U00096.3 genome, we performed gene-level quantitation with `htseq-count` [85], using `union` mode for scoring and `all` mode for non-unique assignments (appropriate for polycistronic mRNAs where a single read is often expected to span multiple genes). Differential expression calling was then performed using deseq2 with default settings; separate models were fitted for comparison of WT/*ihf*/*hns stpA* cells, WT/*fis*/*hfq* cells, and the time course for 5-KDG exposure.

HMM classes

HMM fits were performed using the hmmlearn python package (version 0.2.4) with Gaussian emissions. As input features we used the IPOD-HR robust z scores and RNA polymerase log2(extracted/input) ratios, for a total of 2 features per condition at each of 928,330 sites on the genome (5 bp resolution). We trained a series of HMMs using 20-fold cross validation (dividing the genome into 20 evenly sized blocks), in which we assessed the log-likelihoods for the withheld folds based on an HMM trained on the rest of the genome. After training and evaluating

models from 2 to 20 components, we found that the predictive performance increased sharply with component count up to 6 components, and after that increased much more gradually. We thus used a six-component model to provide a balance of interpretability and predictive performance. We fitted 20 final models using the entire genome and selected the one with the highest likelihood to provide the final HMM; state assignments were then obtained using the Viterbi algorithm. Default parameters for hmmlearn were used unless otherwise noted.

Hfq binding was measured by cloning Hfq-PAmCherry from [60] into MG1655 (2) and performing ChIP-seq with a monoclonal mCherry antibody (Thermo Fisher M11217) (*manuscript in press*). A 500 bp rolling mean of the $\log_2$ extracted/input ratio was calculated and used for comparison in this paper.

Data visualization and analysis

For data analysis as previously described [12], we made heavy use of numpy [12,86], R version 3.6.3 [87,88], tidyverse [89], and ggplot2[90].

Data Availability

RNA-Seq, IPOD-HR, DNA Sequencing, and ChIP-seq data: Gene Expression Omnibus GSE164796 (https://www.ncbi.nlm.nih.gov/geo/query/acc.cgi?acc=GSE164796)

Acknowledgments

This work was supported by NIH grants R00-GM097033 and R35-GM128637 (to PLF) and NSF grant MCB 1714539 (to LS).

Author Contributions

Conceptualization, H.M.A .and P.L.F.; Methodology, H.M.A., T.G., and P.L.F; Investigation, H.M.A., T.G., T.N., L.A.S., R.H., and P.L.F.; Data Analysis and Curation, H.M.A. and P.L.F.; Writing -- Original Draft, H.M.A., T.N., L.A.S., and P.L.F.; Funding Acquisition, L.S. and P.L.F.

Conflict of interests

The authors have no competing interests.

References

1. Shen BA, Landick R. Transcription of Bacterial Chromatin. Journal of Molecular Biology. 2019. pp. 4040–4066. doi:10.1016/j.jmb.2019.05.041
2. Luijsterburg MS, White MF, van Driel R, Dame RT. The major architects of chromatin: architectural proteins in bacteria, archaea and eukaryotes. Crit Rev Biochem Mol Biol. 2008;43: 393–418.
3. Dillon SC, Dorman CJ. Bacterial nucleoid-associated proteins, nucleoid structure and gene expression. Nat Rev Microbiol. 2010;8: 185–195.
4. Postow L, Hardy CD, Arsuaga J, Cozzarelli NR. Topological domain structure of the Escherichia coli chromosome. Genes Dev. 2004;18: 1766–1779.
5. Deng S, Stein RA, Higgins NP. Organization of supercoil domains and their reorganization by transcription. Mol Microbiol. 2005;57: 1511–1521.
6. Boudreau BA, Hron DR, Qin L, van der Valk RA, Kotlajich MV, Dame RT, Landick R. StpA and Hha stimulate pausing by RNA polymerase by promoting DNA-DNA bridging of H-NS filaments. Nucleic Acids Res. 2018;46: 5525–5546.
7. Lim CJ, Whang YR, Kenney LJ, Yan J. Gene silencing H-NS paralogue StpA forms a rigid protein filament along DNA that blocks DNA accessibility. Nucleic Acids Res. 2012;40: 3316–3328.

8. Grainger DC, Goldberg MD, Lee DJ, Busby SJW. Selective repression by Fis and H-NS at the Escherichia coli dps promoter. Mol Microbiol. 2008;68: 1366–1377.

9. Ali Azam T, Iwata A, Nishimura A, Ueda S, Ishihama A. Growth phase-dependent variation in protein composition of the Escherichia coli nucleoid. J Bacteriol. 1999;181: 6361–6370.

10. Amemiya HM, Schroeder J, Freddolino PL. Nucleoid-associated proteins shape chromatin structure and transcriptional regulation across the bacterial kingdom. Transcription. 2021; 1–37.

11. Vora T, Hottes AK, Tavazoie S. Protein occupancy landscape of a bacterial genome. Mol Cell. 2009;35: 247–253.

12. Freddolino PL, Goss TJ, Amemiya HM, Tavazoie S. Dynamic landscape of protein occupancy across the Escherichia coli chromosome. doi:10.1101/2020.01.29.924811

13. Freddolino PL, Amemiya HM, Goss TJ, Tavazoie S. Dynamic landscape of protein occupancy across the Escherichia coli chromosome. PLoS Biol. 2021;19: e3001306.

14. Ueguchi C, Mizuno T. The Escherichia coli nucleoid protein H-NS functions directly as a transcriptional repressor. EMBO J. 1993;12: 1039–1046.

15. Singh SS, Singh N, Bonocora RP, Fitzgerald DM, Wade JT, Grainger DC. Widespread suppression of intragenic transcription initiation by H-NS. Genes Dev. 2014;28: 214–219.

16. Kotlajich MV, Hron DR, Boudreau BA, Sun Z, Lyubchenko YL, Landick R. Bridged filaments of histone-like nucleoid structuring protein pause RNA polymerase and aid termination in bacteria. Elife. 2015;4. doi:10.7554/eLife.04970

17. Landick R, Wade JT, Grainger DC. H-NS and RNA polymerase: a love-hate relationship? Curr Opin Microbiol. 2015;24: 53–59.

18. van der Valk RA, Vreede J, Qin L, Moolenaar GF, Hofmann A, Goosen N, Dame RT. Mechanism of environmentally driven conformational changes that modulate H-NS DNA-bridging activity. Elife. 2017;6. doi:10.7554/eLife.27369

19. Lucchini S, Rowley G, Goldberg MD, Hurd D, Harrison M, Hinton JCD. H-NS mediates the silencing of laterally acquired genes in bacteria. PLoS Pathog. 2006;2: e81.

20. Kahramanoglou C, Seshasayee ASN, Prieto AI, Ibberson D, Schmidt S, Zimmermann J, Benes V, Fraser GM, Luscombe NM. Direct and indirect effects of H-NS and Fis on global gene expression control in Escherichia coli. Nucleic Acids Res. 2011;39: 2073–2091.

21. Baumler A. Faculty Opinions recommendation of Selective silencing of foreign DNA with low GC

content by the H-NS protein in Salmonella. Faculty Opinions – Post-Publication Peer Review of the Biomedical Literature. 2006. doi:10.3410/f.1032929.492954

22. Navarre WW. Selective Silencing of Foreign DNA with Low GC Content by the H-NS Protein in Salmonella. Science. 2006. pp. 236–238. doi:10.1126/science.1128794

23. Scholz SA, Diao R, Wolfe MB, Fivenson EM, Lin XN, Freddolino PL. High-Resolution Mapping of the Escherichia coli Chromosome Reveals Positions of High and Low Transcription. Cell Syst. 2019;8: 212–225.e9.

24. Nakamura K, Ogura Y, Gotoh Y, Hayashi T. Prophages integrating into prophages: a mechanism to accumulate type III secretion effector genes and duplicate Shiga toxin-encoding prophages in Escherichia coli. doi:10.1101/2020.11.04.367953

25. Remesh SG, Verma SC, Chen J-H, Ekman AA, Larabell CA, Adhya S, Hammel M. Nucleoid remodeling during environmental adaptation is regulated by HU-dependent DNA bundling. Nat Commun. 2020;11: 2905.

26. Verma SC, Qian Z, Adhya SL. Correction: Architecture of the Escherichia coli nucleoid. PLoS Genet. 2020;16: e1009148.

27. Neeli-Venkata R, Martikainen A, Gupta A, Gonçalves N, Fonseca J, Ribeiro AS. Robustness of the Process of Nucleoid Exclusion of Protein Aggregates in Escherichia coli. J Bacteriol. 2016;198: 898–906.

28. Small Things Considered. [cited 25 Dec 2020]. Available: https://schaechter.asmblog.org/schaechter/2009/11/the-limitations-of-lb-medium.html

29. Neidhardt FC, Bloch PL, Smith DF. Culture Medium for Enterobacteria. Journal of Bacteriology. 1974. pp. 736–747. doi:10.1128/jb.119.3.736-747.1974

30. Freddolino PL, Amini S, Tavazoie S. Newly identified genetic variations in common Escherichia coli MG1655 stock cultures. J Bacteriol. 2012;194: 303–306.

31. Goodarzi H, Elemento O, Tavazoie S. Revealing global regulatory perturbations across human cancers. Mol Cell. 2009;36: 900–911.

32. Hengge R. Principles of c-di-GMP signalling in bacteria. Nat Rev Microbiol. 2009;7: 263–273.

33. Sanchez-Torres V, Hu H, Wood TK. GGDEF proteins YeaI, YedQ, and YfiN reduce early biofilm formation and swimming motility in Escherichia coli. Appl Microbiol Biotechnol. 2011;90: 651–658.

34. Santos-Zavaleta A, Pérez-Rueda E, Sánchez-Pérez M, Velázquez-Ramírez DA, Collado-Vides J.

Tracing the phylogenetic history of the Crl regulon through the Bacteria and Archaea genomes. BMC Genomics. 2019;20: 299.

35. Wang L, Reeves PR. Organization of Escherichia coli O157 O antigen gene cluster and identification of its specific genes. Infect Immun. 1998;66: 3545–3551.

36. D'Souza JM, Wang L, Reeves P. Sequence of the Escherichia coli O26 O antigen gene cluster and identification of O26 specific genes. Gene. 2002. pp. 123–127. doi:10.1016/s0378-1119(02)00876-4

37. Feng L, Han W, Wang Q, Bastin DA, Wang L. Characterization of Escherichia coli O86 O-antigen gene cluster and identification of O86-specific genes. Veterinary Microbiology. 2005. pp. 241–248. doi:10.1016/j.vetmic.2004.12.021

38. Nakao R, Ramstedt M, Wai SN, Uhlin BE. Enhanced biofilm formation by Escherichia coli LPS mutants defective in Hep biosynthesis. PLoS One. 2012;7: e51241.

39. Linkevicius M, Sandegren L, Andersson DI. Mechanisms and fitness costs of tigecycline resistance in Escherichia coli. J Antimicrob Chemother. 2013;68: 2809–2819.

40. Wang Z, Wang J, Ren G, Li Y, Wang X. Deletion of the genes waaC, waaF, or waaG in Escherichia coli W3110 disables the flagella biosynthesis. J Basic Microbiol. 2016;56: 1021–1035.

41. Rubirés X, Saigi F, Piqué N, Climent N, Merino S, Albertí S, Tomás JM, Regué M. A gene (wbbL) from Serratia marcescens N28b (O4) complements the rfb-50 mutation of Escherichia coli K-12 derivatives. J Bacteriol. 1997;179: 7581–7586.

42. Frenkiel-Krispin D, Levin-Zaidman S, Shimoni E, Wolf SG, Wachtel EJ, Arad T, et al. Regulated phase transitions of bacterial chromatin: a non-enzymatic pathway for generic DNA protection. EMBO J. 2001;20: 1184–1191.

43. Nair S, Finkel SE. Dps protects cells against multiple stresses during stationary phase. J Bacteriol. 2004;186: 4192–4198.

44. Salgado H, Martínez-Flores I, Bustamante VH, Alquicira-Hernández K, García-Sotelo JS, García-Alonso D, Collado-Vides J. Using RegulonDB, the Escherichia coli K-12 Gene Regulatory Transcriptional Network Database. Curr Protoc Bioinformatics. 2018;61: 1.32.1–1.32.30.

45. Bausch C, Ramsey M, Conway T. Transcriptional organization and regulation of the L-idonic acid pathway (GntII system) in Escherichia coli. J Bacteriol. 2004;186: 1388–1397.

46. Gómez KM, Rodríguez A, Rodriguez Y, Ramírez AH, Istúriz T. The subsidiary GntII system for gluconate metabolism in Escherichia coli: alternative induction of the gntV gene. Biol Res. 2011;44:

269–275.

47. Bausch C, Peekhaus N, Utz C, Blais T, Murray E, Lowary T, et al. Sequence analysis of the GntII (subsidiary) system for gluconate metabolism reveals a novel pathway for L-idonic acid catabolism in Escherichia coli. J Bacteriol. 1998;180: 3704–3710.

48. Barh D, Azevedo V. Omics Technologies and Bio-engineering: Volume 1: Towards Improving Quality of Life. Academic Press; 2017.

49. Francis NJ, Kingston RE. Mechanisms of transcriptional memory. Nature Reviews Molecular Cell Biology. 2001. pp. 409–421. doi:10.1038/35073039

50. Lagha M, Ferraro T, Dufourt J, Radulescu O, Mantovani M. Transcriptional Memory in the Drosophila Embryo. Mechanisms of Development. 2017. p. S137. doi:10.1016/j.mod.2017.04.382

51. Palozola KC, Lerner J, Zaret KS. A changing paradigm of transcriptional memory propagation through mitosis. Nat Rev Mol Cell Biol. 2019;20: 55–64.

52. Kundu S, Horn PJ, Peterson CL. SWI/SNF is required for transcriptional memory at the yeast GAL gene cluster. Genes Dev. 2007;21: 997–1004.

53. Moazed D. Mechanisms for the inheritance of chromatin states. Cell. 2011;146: 510–518.

54. Wang X, Kim Y, Ma Q, Hong SH, Pokusaeva K, Sturino JM, Wood TK. Cryptic prophages help bacteria cope with adverse environments. Nat Commun. 2010;1: 147.

55. Hong SH, Wang X, Wood TK. Controlling biofilm formation, prophage excision and cell death by rewiring global regulator H-NS of Escherichia coli. Microb Biotechnol. 2010;3: 344–356.

56. Faubladier M, Bouché JP. Division inhibition gene dicF of Escherichia coli reveals a widespread group of prophage sequences in bacterial genomes. J Bacteriol. 1994;176: 1150–1156.

57. Nagai K. Faculty Opinions recommendation of Hfq: a bacterial Sm-like protein that mediates RNA-RNA interaction. Faculty Opinions – Post-Publication Peer Review of the Biomedical Literature. 2002. doi:10.3410/f.1003709.40104

58. Valentin-Hansen P, Eriksen M, Udesen C. The bacterial Sm-like protein Hfq: a key player in RNA transactions. Molecular Microbiology. 2004. pp. 1525–1533. doi:10.1111/j.1365-2958.2003.03935.x

59. Orans J, Kovach AR, Hoff KE, Horstmann NM, Brennan RG. Crystal structure of an Escherichia coli Hfq Core (residues 2–69)–DNA complex reveals multifunctional nucleic acid binding sites. Nucleic Acids Research. 2020. pp. 3987–3997. doi:10.1093/nar/gkaa149

60. McQuail J, Switzer A, Burchell L, Wigneshweraraj S. The RNA-binding protein Hfq assembles into foci-like structures in nitrogen starved. J Biol Chem. 2020;295: 12355–12367.

61. Bokal AJ 4th, Ross W, Gourse RL. The transcriptional activator protein FIS: DNA interactions and cooperative interactions with RNA polymerase at the Escherichia coli rrnB P1 promoter. J Mol Biol. 1995;245: 197–207.

62. Appleman JA, Ross W, Salomon J, Gourse RL. Activation of Escherichia coli rRNA transcription by FIS during a growth cycle. J Bacteriol. 1998;180: 1525–1532.

63. Chintakayala K, Singh SS, Rossiter AE, Shahapure R, Dame RT, Grainger DC. E. coli Fis protein insulates the cbpA gene from uncontrolled transcription. PLoS Genet. 2013;9: e1003152.

64. Cho B-K, Knight EM, Barrett CL, Palsson BØ. Genome-wide analysis of Fis binding in Escherichia coli indicates a causative role for A-/AT-tracts. Genome Res. 2008;18: 900–910.

65. Updegrove TB, Zhang A, Storz G. Hfq: the flexible RNA matchmaker. Curr Opin Microbiol. 2016;30: 133–138.

66. Link AJ, Phillips D, Church GM. Methods for generating precise deletions and insertions in the genome of wild-type Escherichia coli: application to open reading frame characterization. Journal of bacteriology. 1997. pp. 6228–6237. doi:10.1128/jb.179.20.6228-6237.1997

67. Posfai G. Emergent Properties of Reduced-Genome Escherichia coli. Science. 2006. pp. 1044–1046. doi:10.1126/science.1126439

68. Albano M, Smits WK, Ho LTY, Kraigher B, Mandic-Mulec I, Kuipers OP, Dubnau D. The Rok Protein of Bacillus subtilis Represses Genes for Cell Surface and Extracellular Functions. J Bacteriol. 2005;187: 2010.

69. Hoa TT, Tortosa P, Albano M, Dubnau D. Rok (YkuW) regulates genetic competence in Bacillus subtilis by directly repressing comK. Mol Microbiol. 2002;43. doi:10.1046/j.1365-2958.2002.02727.x

70. Wiep Klaas Smits ADG. The Transcriptional Regulator Rok Binds A+T-Rich DNA and Is Involved in Repression of a Mobile Genetic Element in Bacillus subtilis. PLoS Genet. 2010;6. doi:10.1371/journal.pgen.1001207

71. Graumann PL. Bacillus subtilis SMC Is Required for Proper Arrangement of the Chromosome and for Efficient Segregation of Replication Termini but Not for Bipolar Movement of Newly Duplicated Origin Regions. J Bacteriol. 2000;182: 6463–6471.

72. Sullivan NL, Marquis KA, Rudner DZ. Recruitment of SMC to the origin by ParB-parS organizes the

origin and promotes efficient chromosome segregation. Cell. 2009;137: 697.

73. Wilhelm L, Bürmann F, Minnen A, Shin H-C, Toseland CP, Oh B-H, Gruber S. SMC condensin entraps chromosomal DNA by an ATP hydrolysis dependent loading mechanism in Bacillus subtilis. 2015 [cited 7 Nov 2020]. doi:10.7554/eLife.06659

74. Al-Bassam MM, Moyne O, Chapin N, Zengler K. Nucleoid openness profiling links bacterial genome structure to phenotype. doi:10.1101/2020.05.07.082990

75. Wasim A, Gupta A, Mondal J. Mapping the Multiscale Organisation of Escherichia Coli Chromosome in a Hi-C-integrated Model. doi:10.1101/2020.06.29.178194

76. Lioy VS, Cournac A, Marbouty M, Duigou S, Mozziconacci J, Espéli O, Boccard F, Koszul R. Multiscale Structuring of the E. coli Chromosome by Nucleoid-Associated and Condensin Proteins. Cell. 2018. pp. 771–783.e18. doi:10.1016/j.cell.2017.12.027

77. Walker DM, Freddolino PL, Harshey RM. A Well-Mixed E. coli Genome: Widespread Contacts Revealed by Tracking Mu Transposition. Cell. 2020;180: 703–716.e18.

78. Shin J-E, Lin C, Lim HN. Horizontal transfer of DNA methylation patterns into bacterial chromosomes. Nucleic Acids Res. 2016;44: 4460–4471.

79. Freddolino PL, Tavazoie S. Beyond Homeostasis: A Predictive-Dynamic Framework for Understanding Cellular Behavior. Annual Review of Cell and Developmental Biology. 2012. pp. 363–384. doi:10.1146/annurev-cellbio-092910-154129

80. Deatherage, DE, Barrick, JE. Identification of mutations in laboratory-evolved microbes from next-generation sequencing data using breseq. Methods Mol. Biol. 2014; 1151: 165–188.

81. Thomason LC, Costantino N, Court DL. E. coli genome manipulation by P1 transduction. Curr Protoc Mol Biol. 2007;Chapter 1: Unit 1.17.

82. Baba T, Ara T, Hasegawa M, Takai Y, Okumura Y, Baba M, et al. Construction of Escherichia coli K-12 in-frame, single-gene knockout mutants: the Keio collection. Mol Syst Biol. 2006;2: 2006.0008.

83. Cherepanov PP, Wackernagel W. Gene disruption in Escherichia coli: TcR and KmR cassettes with the option of Flp-catalyzed excision of the antibiotic-resistance determinant. Gene. 1995;158: 9–14.

84. Jeremy W. Schroeder LAS. Complete Genome Sequence of Bacillus subtilis Strain PY79. Genome Announc. 2013;1. doi:10.1128/genomeA.01085-13

85. Anders S, Pyl PT, Huber W. HTSeq--a Python framework to work with high-throughput sequencing data. Bioinformatics. 2015;31: 166–169.

86. Harris CR, Millman KJ, van der Walt SJ, Gommers R, Virtanen P, Cournapeau D, et al. Array programming with NumPy. Nature. 2020;585: 357–362.

87. Verzani J. Getting Started with RStudio: An Integrated Development Environment for R. “O’Reilly Media, Inc.”; 2011.

88. RStudio. [cited 27 Dec 2020]. Available: https://rstudio.com/

89. Tidyverse. [cited 27 Dec 2020]. Available: https://www.tidyverse.org/

90. Wickham H. ggplot2: Elegant Graphics for Data Analysis. Springer Science & Business Media; 2009.

91. Salvatier J., Wiecki T.V., Fonnesbeck C. Probabilistic programming in Python using PyMC3. PeerJ Computer Science. 2016; 2:e55

Figure Legends

Figure 1: EPODs are highly robust across growth conditions.
(A) Example regions exhibiting the IPOD-HR occupancy where EPOD calls are made. Loose EPODs (pink) and Strict EPODs (teal) represent spans of high protein occupancy at lower and higher thresholds, respectively. Neighboring areas showing lower robust z scores are not EPODs. Note that following the definitions in [12], the presence of an EPOD requires a sustained region of high average occupancy, without any regions in which occupancy drops to background levels. Thus, breaks in EPOD calls represent cases where a rolling average occupancy drops below the calling threshold (e.g., the breakpoint in the middle of *pinQ* in the top panel), and regions of apparent occupancy may nevertheless not be called due to being below the minimum length threshold (as is the case for *nohA*).
(B) Strict EPOD counts across WT (MG1655) *E. coli* cells are similar across different conditions. Cells were grown in: Rich (Rich Defined Media (See Materials and Methods)), Min (Minimal Media) and collected at log phase growth or deep stationary phase (Deep Stat.). WT (2) is a MG1655 isolate from another laboratory that differs from our WT strain by four-point mutations and two insertion sequence integrations.

(C) Fractional coverage of Strict EPODs across the genome does not largely vary across conditions, however cells grown in the Min condition have a slightly larger coverage.
(D) To assess the similarity between EPOD calls in each condition, we calculated the symmetrized overlap distance of EPODs. A value of 0 indicates that the set of EPODs are identical. Hierarchical clustering reveals that growth phase impacts EPOD location in this dataset.
(E) Specific locations across all conditions remain occupied by protein where EPODs across a representative region, the *waa* operon, were called (left) and unoccupied by RNA polymerase (right). The quantile normalized robust z scores of the protein occupancy at each 5 bp are represented by the IPOD-HR occupancy.
(**F)** Kernel density plots displaying the normalized histograms (smoothed by a kernel density estimator) of H-NS ChIP [20] for regions of the genome within EPODs versus Background (*i.e.*, protein occupancy through the rest of the genome, where contiguous regions between EPODs were treated as a single data point). H-NS binding shows a strong overlap with EPOD locations measured in all conditions. (*) indicates FDR-corrected $p<0.005$ via permutation test indicating an enrichment in H-NS ChIP binding in EPODs across conditions (against a null hypothesis of no difference in medians).

Figure 2: Loss of nucleoid associated proteins (NAPs) leads to changes in EPODs.
(A) Number of EPODs called in different NAP deletions. D.S. denotes genotypes where cells were collected in the deep stationary phase of growth.
(B) Fractional coverage of EPODs for each genotype across the genome.
(C) Symmetrized overlap statistic comparing each pair of samples in the NAP deletion dataset. The symmetrized overlap denotes similarity between EPOD locations, where a value of 0 = identical. Hierarchical clustering was performed to group like-genotypes.
(D) Distributions of mean protein occupancy at WT EPOD boundaries and background. The blue dots denote the median and the black line displays the interquartile ranges in each condition. The dashed pink line represents the WT median. (*) indicate the Wilcoxon Rank Sum test p value comparing the change in pseudomedian vs. WT for each condition that has been adjusted using the Benjamini and Hochberg method (against a null hypothesis of no difference in pseudomedians). The grey line denotes the same comparison between the D.S. conditions. Underlined (*)'s indicate a gain in the pseudomedian compared to baseline conditions, while no

underline indicates a loss in the pseudomedian compared to baseline conditions. p value < 0.05 = *, <0.005=**, <0.0005=***. Three biological replicates were used for the “WT, Rich” case and “WT (deep stat.)” case, and two biological replicates for the “WT, Min” and “WT (2), Rich” conditions.

(E) Protein occupancy over the *waa* operon. The quantile normalized robust z scores of the protein occupancy at each 5 bp are represented by the IPOD-HR occupancy. The EPOD over the waa operon is lost in the *ΔstpAΔhns* condition which results in increased accessibility and RNA polymerase occupancy (**Fig. S3A**).

(F) The loss in protein occupancy shown in Figure 2E leads to increases in RNA polymerase occupancy across the *waa* operon.

Figure 3: Changes in EPODs are induced in specific conditions.

(A) Experimental overview. WT, MG1655 cells were grown in M9 Minimal Media with 0.2% glucose, samples were collected at mid log phase of growth (OD_{600} ~0.2) for RNA-seq and IPOD-HR. The cells were back diluted to an OD_{600} of ~0.1 in M9 Minimal Media with 0.2% 5-Keto-D-gluconic-acid (5KDG), grown to an OD_{600} of ~0.2, collected for RNA-seq and IPOD-HR. In the final shift, the cells were back diluted to an OD_{600} of ~0.003 in M9 Minimal Media with 0.2% glucose, grown to OD_{600} of 0.2 and collected for RNA-seq and IPOD-HR. Two biological replicates were performed.

(B) Protein occupancy over the *idn* operon for each condition (colors are denoted in (**A**)). The quantile normalized robust z scores of the protein occupancy at each 5 bp are represented by the IPOD-HR occupancy. There is a large loss in protein occupancy when cells are shifted to 5KDG, leading to the loss of the call
ed EPOD. Protein occupancy is restored once cells are grown in the second glucose condition. The 500bp normalized average of previously published H-NS ChIP-seq [20] exhibits high H-NS binding on the idnD promoter region.

(C) To examine the expression of the idn operon at each shift, RNA-seq was performed. RNA-seq expression estimates $\log_2$ scaled for *idn* operon genes for WT cells grown in each condition (as colored in (**A**)). Comparisons are denoted with colored dots with significance stars representing the adjusted p-value where (***) signify q-values <0.0005 (called using DeSeq2, as described in Methods).

Commented [HG1]: Please define the statistical test.

(D) Spearman correlations are represented with the heatmap comparing the expression profiles in each condition, where identical expression values for every gene show a spearman correlation of 1. The symmetrized overlap distance was calculated for all EPODs for each condition, where a value of 0 is identical. The colored squares on the sides of the heatmaps denote the condition (following the colors shown in (**A**)).

Figure 4: EPODs mediate transcriptional memory.

(A) Schematic of KDG competition experiments. Day -1: both the WT (red) and *lacZ::cat* (blue) are grown overnight (O/N) in M9 Min Glucose. They are back diluted together in M9 Min Glucose (yellow) and M9 Min KDG (orange). Serial dilutions of each media condition were spotted both immediately after inoculation and after 48hrs of growth at 37 C. Day 0: The WT cells grown O/N in glucose from Day 0 were back diluted and grown in M9 Min KDG for 48 hrs - these cells are now "KDG Adapted". These cells were then competed against fresh *lacZ::cat* that were grown in M9 Min Glucose O/N. A mixture of both of these cells were placed in M9 Min Glu and M9 Min KDG, and spotted as previously described in Day 0. Day 1: The WT "KDG Adapted" cells grown in M9 Min KDG for 48 hrs were back diluted into M9 Min Glu and grown for 12 or 24 hrs (in separate cultures). As with Day 0, these cells were then competed against fresh *lacZ::cat* that were grown in M9 Min Glucose O/N: A mixture of these cells was placed in M9 Min Glu and M9 Min KDG, and spotted as previously described in Day 0, and recorded as Day 0.5 (12 hours outgrowth in M9 Min Glu) and Day 1 (24 hours outgrowth in M9 Min Glu). The subsequent timepoints shown in **(B)** indicate the time KDG Adapted cells were grown in M9 Min Glu after they were KDG Adapted (*i.e.,* Day 2 = 48hrs, Day 3 = 72 hours; fresh back-dilutions were performed every 24 hours from the previous M9 Min Glu culture). All later timepoints follow the same workflow as that shown for Day 1, beginning from cells that had been passaged additional times in M9 Min Glu.

(B) Difference in Log_2 ratio of fitnesses of the KDG-exposed cells with unexposed *lacZ::cat* ($\Delta\lambda$; see Materials and Methods) relative to that observed prior to KDG exposure, given as a function of time since exposure to KDG. Day -1 corresponds to the day before KDG exposure, Day 0 is cells taken immediately after growth in KDG, and subsequent timepoints reflect different durations of growth in M9 Min Glu prior to competition (See **(A)**). Points show medians across replicates (3 biological replicates for 0.5 days, 6 biological replicates for all other timepoints); error bars show 95% confidence intervals for the difference relative to the Day -1 timepoint, calculated using the R wilcox.test function. Significance was assessed using a Wilcoxon rank

sum test comparing the distribution at each timepoint to the -1 day (naive) timepoint: *, p<0.05; **, p<0.005. Individual data points are shown in **Appendix Figure S5**.

(C) Lag times for cells grown in glucose, shifted to 5KDG, and then shifted back to glucose. (***) is defined as where the mean posterior probability of difference >0.999, assessed using a Bayesian model (see Materials and Methods for details); data points show the values obtained for three biological replicates. Errors bars show 95% credible intervals.

Figure 5: Nucleoid associated proteins contribute to protein occupancy at EPODs that contain prophages.

(A) IPOD-HR occupancy and RNA polymerase occupancy over a known H-NS silenced prophage in WT (blue) and *Δhns* (red) cells. The quantile normalized robust z scores of the protein occupancy at each 5 bp are represented by the IPOD-HR occupancy.

(B) The mean protein occupancy (IPOD-HR occupancy) was calculated over WT EPOD locations that contain prophages (41 EPOD locations). As in **Fig. 2D,** the blue dots denote the median and the black line displays the interquartile ranges in each condition. The dashed pink line represents the WT median. (*) indicate significance assessed via a Wilcoxon Rank Sum test comparing the change in pseudomedian vs. WT for each condition (against a null hypothesis of no difference in medians), after application of a Benjamini-Hochberg correction for multiple hypothesis testing. The smaller horizontal line denotes the same comparison between the D.S. conditions. Q value < 0.05 = *, <0.005=**, <0.0005=***. Data were averaged across 2 (*hupAB, fis, stpA, ihf, dps*), 3 (WT, *hfq,* WT DS, *dps* DS),or 4 (*hns, stpA/hnS*) biological replicates.

Commented [HG2]: Please define the number and the nature, i.e. biological or technical, of the replicates.

(C) Mean protein occupancy was calculated across all WT EPOD locations that contain annotated prophages. The change in mean protein occupancy compared to WT was calculated for each condition, where anything negative is a loss in occupancy compared to WT. Hierarchical clustering was performed to examine which genotypes clustered together and were more similar. Permutation tests comparing the change in occupancy over EPODs containing prophages were performed against the rest of the genome. P value <0.05 = *, <0.005=** indicate a negative mean change in occupancy compared to WT.

Figure 6: Loss of Fis and Hfq is lethal in a prophage-dependent manner.

(A) Example prophage region that is annotated with the Fis- and Hfq-associated HMM class 5 in our genome-wide HMM classification (**Table 1**). The quantile normalized robust z scores of the protein occupancy at each 5 bp are represented by the IPOD-HR occupancy. Prophage genes

are highlighted with a red box. The major peak associated with WT IPOD-HR occupancy is represented in a grey dashed line as a reference to compare IPOD-HR occupancy in the other genotypes. Modest loss of protein occupancy was observed at the same prophage-containing EPOD for *Δfis* (light purple; see color key in (**B**)) and *Δhfq* (dark purple; see color key in (**B**)) conditions compared to WT (gold).

(B) RNA-seq of WT, *Δfis,* and *Δhfq* were performed. The log fold change compared to WT was calculated at prophage genes contained in the dashed box in (**A**). Induction of prophages across the region where loss in occupancy is observed. (*) indicate the adjusted p-value: <0.10 = +, < 0.05 = *, <0.005=**, <0.0005=*** (calculated using DeSeq2 as described in Methods).

(C) The log fold change of all genes for *Δfis* and *Δhfq* are shown in a hexbin plot. Counts for each gene transcript contained in one bin are denoted with the counts bar.

(D) The log fold change of all prophage genes for *Δfis* and *Δhfq* are shown in a hexbin plot.

(E) Outline of quadrant map to calculate the number of genes that fall within each quadrant for (**F**). The symbols represent log fold changes compared to WT in *Δfis / Δhfq*. For instance, +/+ denotes a positive log fold change in *Δfis* and *Δhfq*, -/+ denotes negative log fold change in *Δfis* and positive in *Δhfq*.

(F) Rate ratios of all genes (grey) and prophage genes (red) in each quadrant outline in (**E**), showing a higher rate of genes that resided in the +/+ category, indicating that many prophages are de-repressed in both *Δfis* and *Δhfq*. (*) indicate the p-value calculated from testing the null that the rate ratios are the same. P-value < 0.05 = *, <0.005=**, <0.0005=*** (calculated using DeSeq2 as described in Methods).

Commented [HG3]: Please define the statistical test.

(G) P1 vir transduction experiment to test the viability of *Δfis* and *Δhfq*. -Hfq indicates deleting Hfq and -CspE indicates deleting -CspE as a control. Strain identities are indicated in the box. Number of transductions were counted on LB + Kan plates; all efficiencies are relative to WT, and thus the log-scaled relative transduction rate for the WT itself is 0 by definition. *-R1* indicates that the prophage region in (**A**) was deleted to test whether the loss of prophages silenced by Fis and Hfq restored viability of a *Δfis Δhfq* genotype. R2 and R3 were other regions in the genome that contained prophages that appeared to have Fis/Hfq dependent EPODs. Plotted values are mean efficiencies across replicates, with error bars showing a 95% credible

interval obtained via Bayesian inference, assuming the replicate-level colony counts are Poisson distributed with a (conjugate) Gamma(0,0) prior; all log ratios (including error bounds) are plotted relative to the mean WT value. Data obtained from 5 biological replicates for *hfq::kan* transductions and 4 biological replicates for *cspE::kan* transductions.

Figure 7: IPOD-HR in *Bacillus subtilis* reveals Rok-bound and SMC-bound domains.
(A) IPOD-HR ChIP-subtracted z-scores and RNA polymerase ChIP in the vicinity of an extended protein occupancy domain (EPOD). ChIP tracks are shown as log2 extracted/input ratios; the z-score is the ChIP-subtracted robust z-score smoothed with a 512 bp rolling median.
(B) IPOD-HR and RNA polymerase ChIP tracks in the vicinity of a negative EPOD (nEPOD).
(C) Effects of deletion of *rok* in the vicinity of an nEPOD; Rok ChIP data from[70] shows a strong overlap with the nEPOD boundary, whereas that occupancy region is lost in Δ*rok* cells.
(D) Distributions of Rok ChIP occupancies (see Materials and Methods) in the EPODs and nEPODs called in WT (top) or Δ*rok* (bottom) cells; note that the Rok ChIP occupancy was taken only in WT cells. (*) indicates a significant difference from the 'neither' distribution (that is, genomic sites that are not in an EPOD or nEPOD); $p<0.05$, permutation test.
(E) Comparison of IPOD occupancy and SMC ChIP occupancy (see Materials and Methods) in the vicinity of several typical EPODs.
(F) Genome-wide distributions of SMC binding in EPODs vs.nEPODs as assessed in WT cells; (*) indicates a significant difference from the background distribution as in panel **D**.

Tables

	Log_2 Ratio Enrichment						**Group-Level Mean**			
HMM Class	**EPODs**	**TFs**	**Prom.**	**IHF**	**Dam**	**Dcm**	**H-NS**	**Hfq**	**Fis**	**HU**
0	-0.95	-3.49	-2.31	-1.12	0.16	0.08	276.55	-0.14	227.68	1.02
1	-0.36	-1.10	-1.17	-1.01	0.09	-0.04	340.21	0.19	231.26	1.07

2	1.36	1.22	-0.054	1.83	-0.65	-0.78	1230.42	0.42	153.19	0.88
3	1.66	-2.52	-4.24	-1.42	-0.15	-0.19	608.69	0.06	196.31	0.92
4	-1.53	-4.03	-2.41	-3.68	0.14	0.30	268.33	-0.36	220.40	0.93
5	0.06	2.14	1.70	2.21	-0.39	-0.35	437.99	0.77	238.11	1.08
Genome Average	----	----	----	----	----	----	422.24	0.03	217.63	0.99

Table 1: HMM class enrichments. Log_2 Ratio Enrichment: The ratio of the number of EPODs or motifs in a given HMM class to the total number of EPODs or motifs was calculated for each HMM class. A chi-squared test was performed, and all categories were significantly associated with each class; values underlined had a p-value <0.05. Group-Level Mean: The 500-bp rolling mean for the binding of each NAP was used to calculate the group-level means for across each HMM class and compared with the overall average for the genome. Permutation based p-values were calculated comparing each class vs. the background. The values underlined had a p-value <0.05.

Region #	Coordinates	Genes	Gene Functions
1	564815-585633	*essD, ybcS, rzpD, rzoD, borD, ybcV, ybcW, nohB*	DLP12 prophage, putative prophage endopeptidase, lysozyme
2	1400247-1482201	*lar, recT, ydaQ, ydaC, intR*	Rac prophage, recombinase, DNA renaturation
3	1627517-1652838	*ynfO, ydfO, gnsB, ynfN, cspI, ydfP, hokD*	Qin prophage, cold shock, toxin anti-toxin system

Table 2: MDS42 regions containing prophages.

Expanded View Figure Legends

Figure EV1: Loss of NAPs results in increases in RNA polymerase occupancy and decreases in overlapping EPODs.

(A) Average RNA polymerase occupancy was calculated across intergenic regions within WT EPODs and background. Similar to Figure 2D, the blue dots denote the median and the black line displays the interquartile ranges in each condition. The dashed pink line represents the WT median. (*) indicate the Wilcoxon Rank Sum p value comparing the change in median vs. WT for each condition that has been adjusted using the Benjamini and Hochberg method (against a null hypothesis of no difference in medians). The grey line denotes the same comparison between the D.S. conditions. P value <0.0005=***. Data were averaged across 2 (*hupAB, fis, stpA, ihf, dps*), 3 (WT, *hfq,* WT DS, *dps* DS),or 4 (*hns, stpA/hnS*) biological replicates.

(B) Similar to Figure 1D, reading left to right: overlap of the relaxed set of EPOD calls (left) over the stringent set of EPOD calls (bottom).

Commented [HG4]: Please define the number and the nature, i.e. biological or technical, of the replicates.

Figure EV2: H-NS and StpA mediate silencing of the idn operon.

(A) Raw IPOD and RNA polymerase ChIP-seq (both vs. input $\log_{10}$ ratios) over the idn operon.

(B) IPOD-HR was performed in rich defined medium (RDM) supplemented with glucose and exhibits a loss of occupancy in the deletion of both *hns* and *stpA*, as well as increased RNA polymerase occupancy.

(C) RNA-seq was performed in parallel and shows $\log_2$ fold change compared to WT of idn operon expression upon deletion of *hns* and *stpA*. (*) indicate adjusted p-value <0.0005=*** (calculated using DeSeq2 as described in Methods).

Figure EV3: Global protein occupancy across prophage EPODs changes with deletion of NAPs.

The average IPOD-HR occupancy (robust z scores) across each of the 41 prophage EPODs of WT and NAP deletions. Each colored dot represents an individual EPOD. Grey lines connect the same EPOD in WT (or WT D.S.) vs NAP deletion to appreciate the change in occupancy for that particular EPOD. The pink dashed line indicates the median of the WT comparison. The dark blue dot indicates the median of the genotype and transparent lines display the interquartile ranges. The summary of these data is displayed as violins in **Figure 5B**. As shown in **Figure 5B,** (*) indicate the Wilcoxon Rank Sum p value comparing the change in pseudomedian vs. WT for each condition that has been adjusted using the Benjamini and Hochberg method (against a null hypothesis of no difference in pseudomedians). The grey line denotes the same comparison between the D.S. conditions. P value < 0.05 = *, <0.0005=***.

Figure EV4: Growth deficiency of *Δfis Δhfq* cells.

WT, MDS42, *Δfis,* and MDS42 *Δfis* cells containing a temperature sensitive plasmid with *hfq* had their genomic copy of *hfq* deleted. Cells were grown in a permissible temperature (30°C), and then shifted to a non-permissible temperature for plasmid replication (42°C), thus removing *hfq* as the plasmid is dropped. The $\log_{10}$ fold change in CFU is displayed. *Δfis* cells were unable to grow with the loss of the temperature sensitive *hfq* plasmid, however, upon deletion of mobile elements and prophages from the genome (MDS42 strain background), viability was restored. Data show fitted values plus 95% credible intervals for a Bayesian analysis, in which the plate counts themselves were treated as Poisson random variables, with rate parameters arising from an initial cell concentration in cells/mL (at the permissive temperature) and then a post-treatment scaling factor applied to that initial concentration. Both parameters were fitted on a log10 scale, with a Uniform (0,15) prior on the initial cell concentrations and Uniform (-10,10) prior on the treatment effect. The treatment effect parameter is plotted as "log10 growth", reflecting the observed growth at 42°C. Fits were based on three biological replicates for each genotype and were performed using pymc3 [91].

Commented [HG5]: Please define the bars and error bars, e.g. mean ± SD. Please define the number and the nature, i.e. biological or technical, of the replicates.

Figure EV5: nEPODs are a biological feature in *Bacillus subtilis*.

(A) Kernel density plots displaying the input read density *Bacillus subtilis* and *Escherichia coli* in regions called as EPODs (orange),nEPODs (green), and Background (yellow).

(B) Assessment of *Escherichia coli* nEPODs compared to other regions. Log_2 Ratio Enrichment: The ratio of the number of TFs, promoters, or motifs in a given category to the total number of TFs, promoters, or motifs. A chi-squared test was performed, and all categories were significantly associated with each class; values underlined had a p-value <0.05. Group-Level Mean: The 500-bp rolling mean for the binding of each NAP was used to calculate the group-level means for across each category and compared with the overall average for the genome. Permutation based p-values were calculated comparing each class vs. the background. The values underlined had a p-value <0.05.

(C) *Escherichia coli* nEPODs overlap highly transcribed gene categories.

(D) Jaccard distance comparing nEPODs called with and without RNA polymerase ChIP-seq subtraction. The high jaccard distance in *Escherichia coli* indicates that nEPODs change dramatically with and without the inclusion RNA polymerase binding, and therefore RNA polymerase associated. However, locations of nEPODs in *Bacillus subtilis* are unchanged with RNA polymerase binding and are distinct, protein occupied regions.

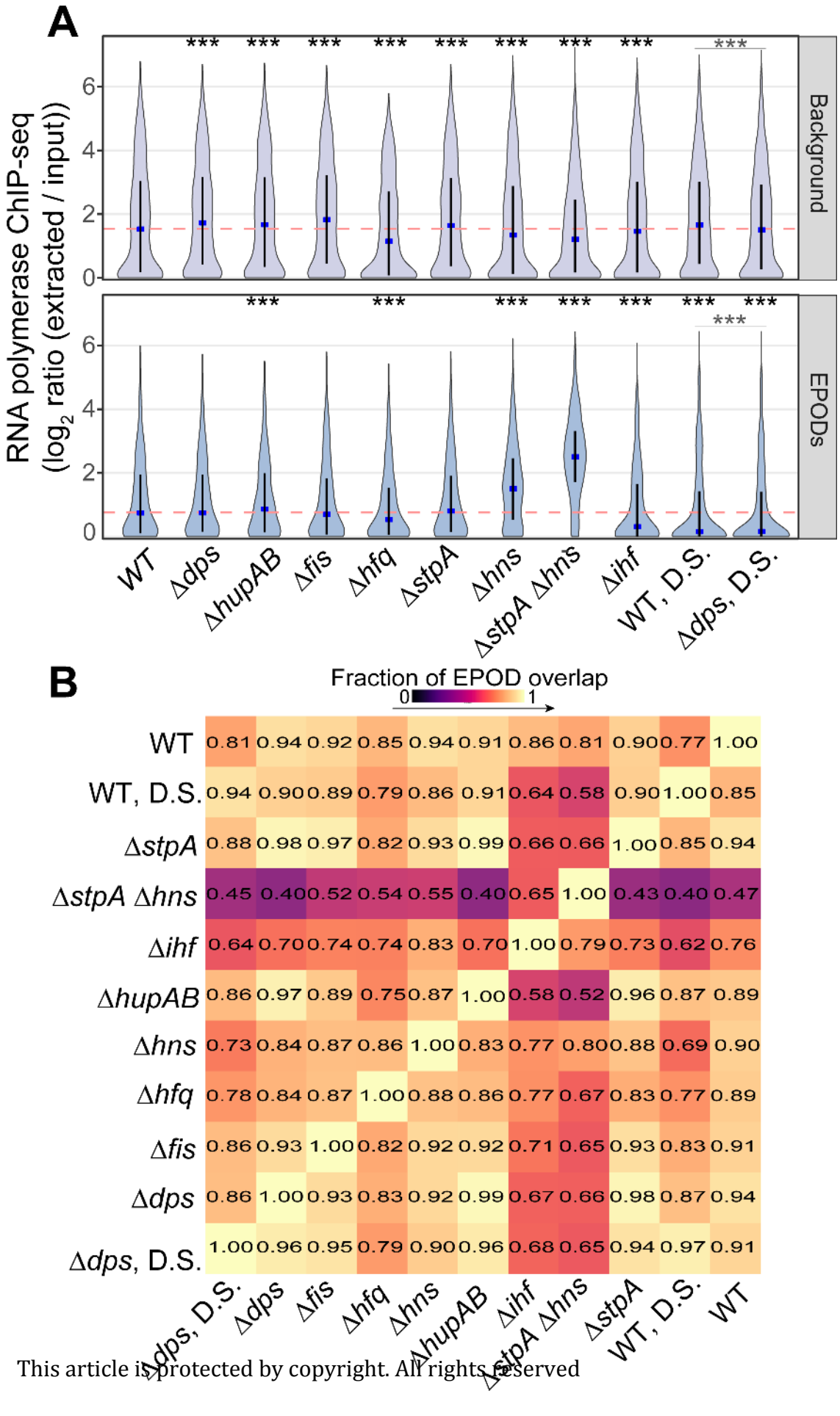

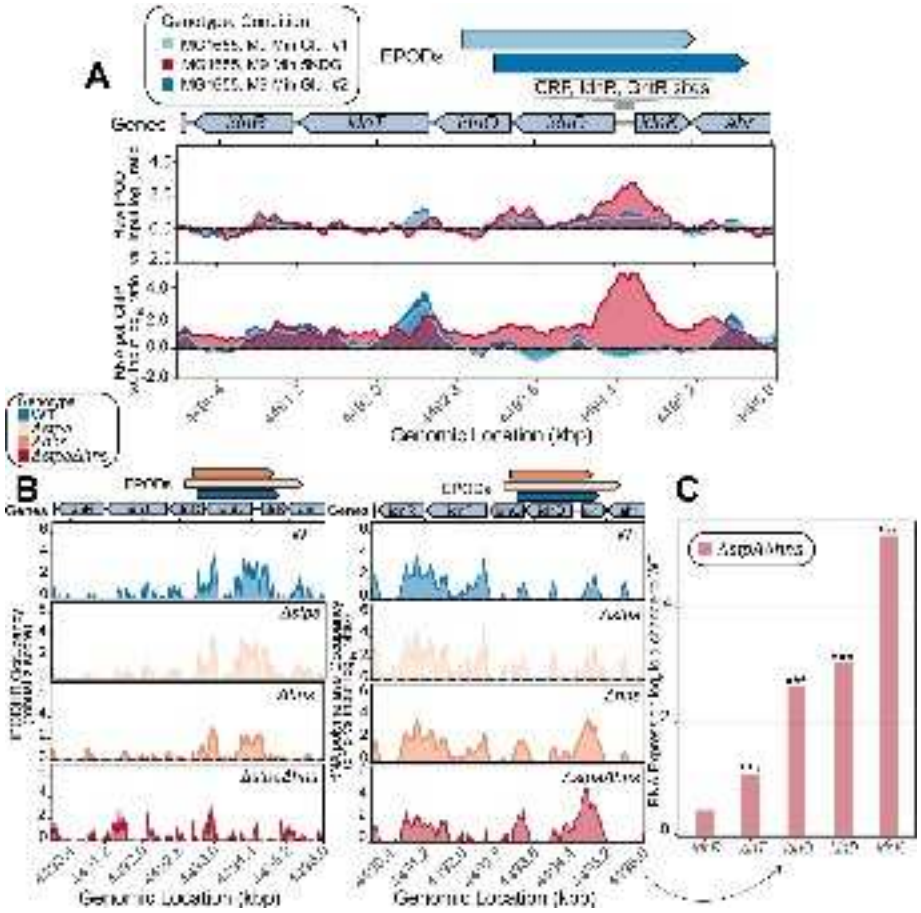

embj_2021108708_fev2.tif

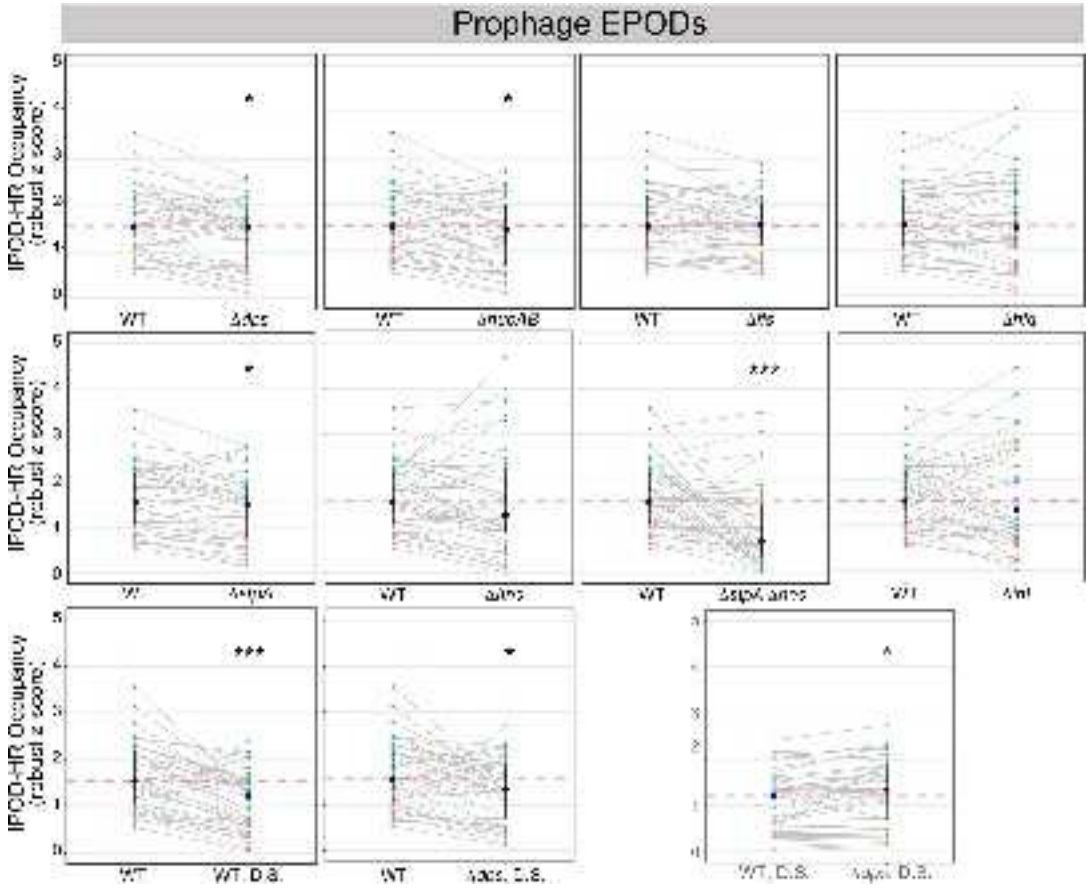

embj_2021108708_fev3.tif

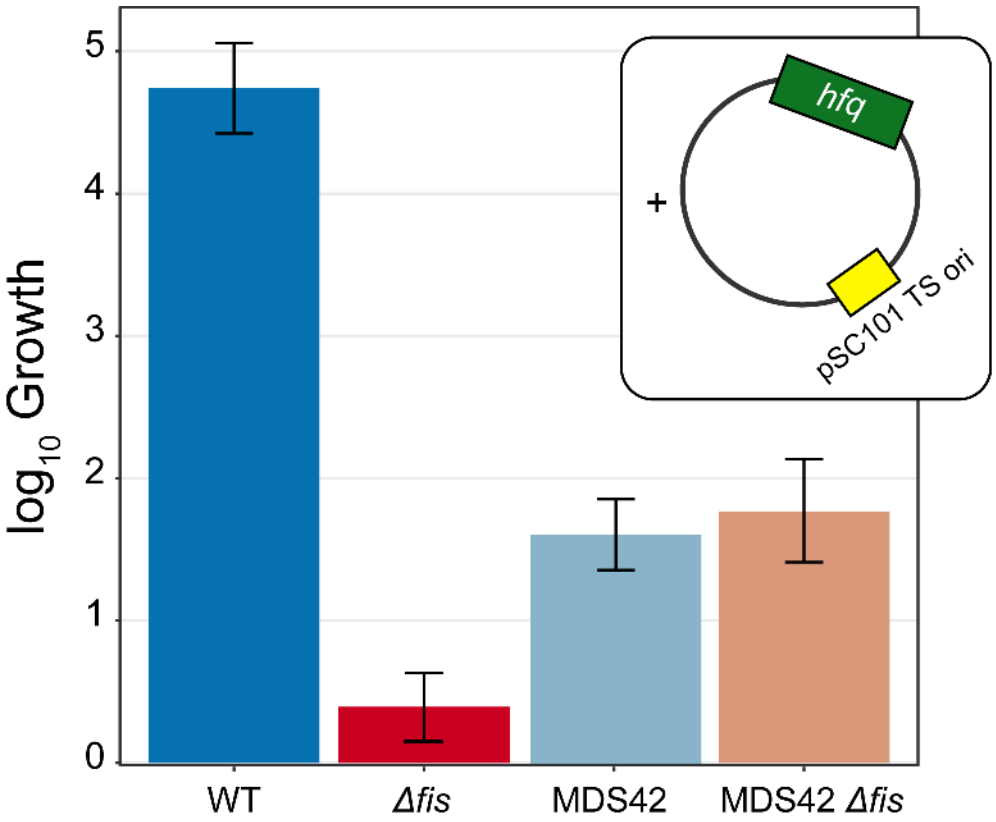

embj_2021108708_fev4.tif

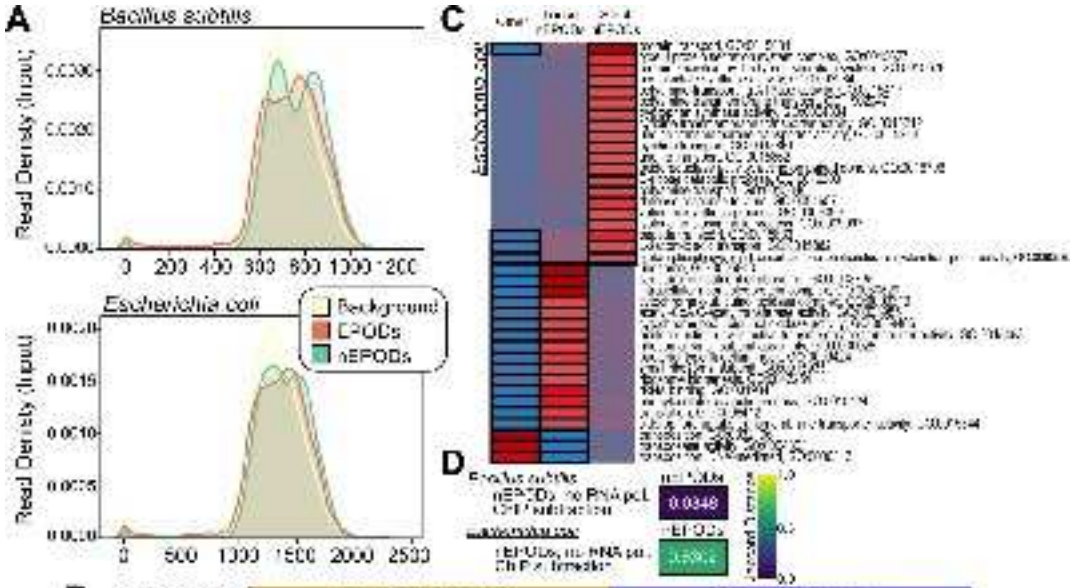

B

Escherichia coli	Log2 Ratio Enrichment					Group-Level Mean				
Category	TFs	Prom	HF	Dom	Dom	H NS	Hq	Fis	HU	AI Codon
Background	-0.06	-0.07	0.10	0.04	0.02	338.12	-0.05	228.10	0.00	0.48
Loose EPODs	0.05	0.19	0.58	0.03	0.14	490.21	0.09	215.74	0.92	0.45
Strict EPODs	0.78	-0.13	0.91	-0.10	-0.17	1213.00	0.31	157.66	0.86	0.56
Leakage EPODs	-1.85	-0.38	0.00	-0.57	-0.74	750.74	0.34	127.03	0.77	0.54
Loose nEPODs	0.21	0.04	0.29	0.16	0.24	279.01	0.15	215.10	1.09	0.50
Strict nEPODs	-0.10	0.25	-1.07	0.16	0.27	236.41	0.10	228.46	1.06	0.49
Genome Average	—	—	—	—	—	422.24	0.03	217.65	0.99	0.49

embj_2021108708_fev5.tif

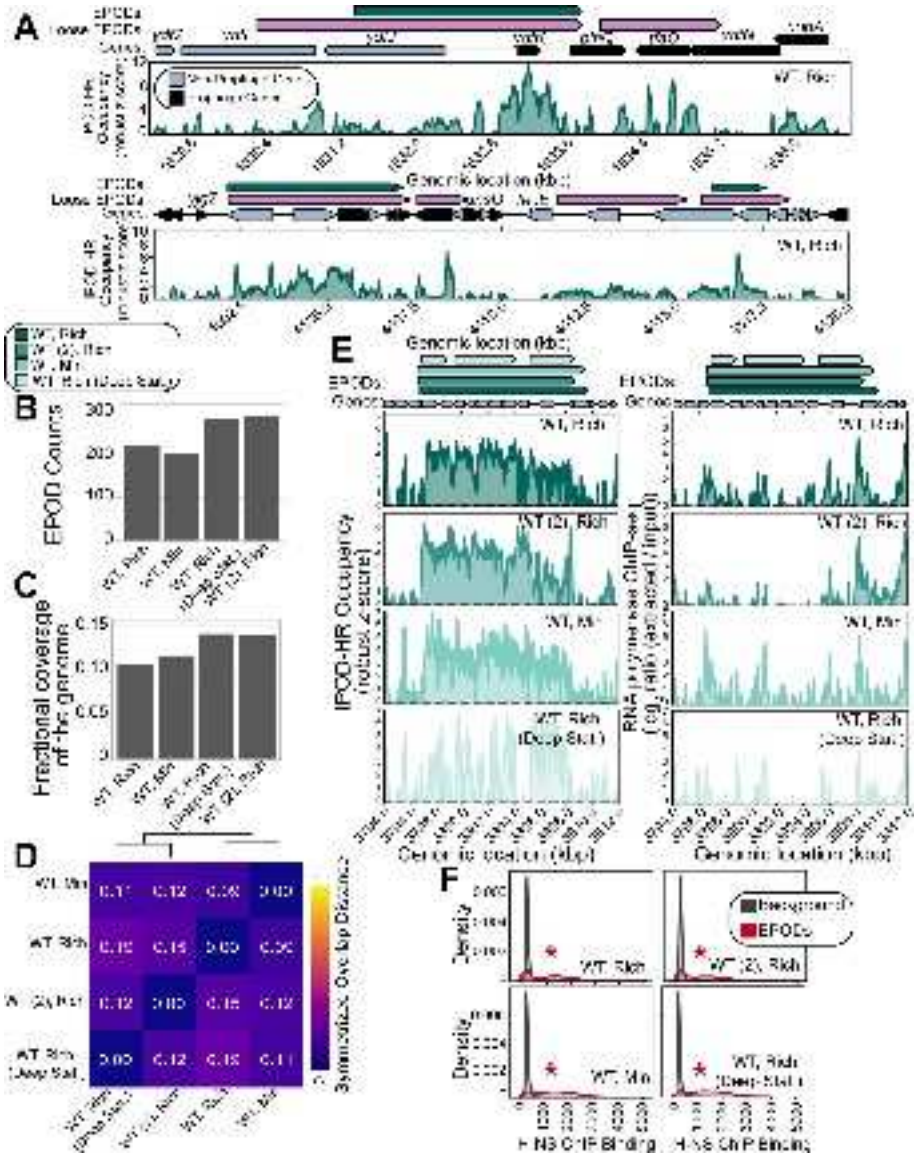

embj_2021108708_f1.tif

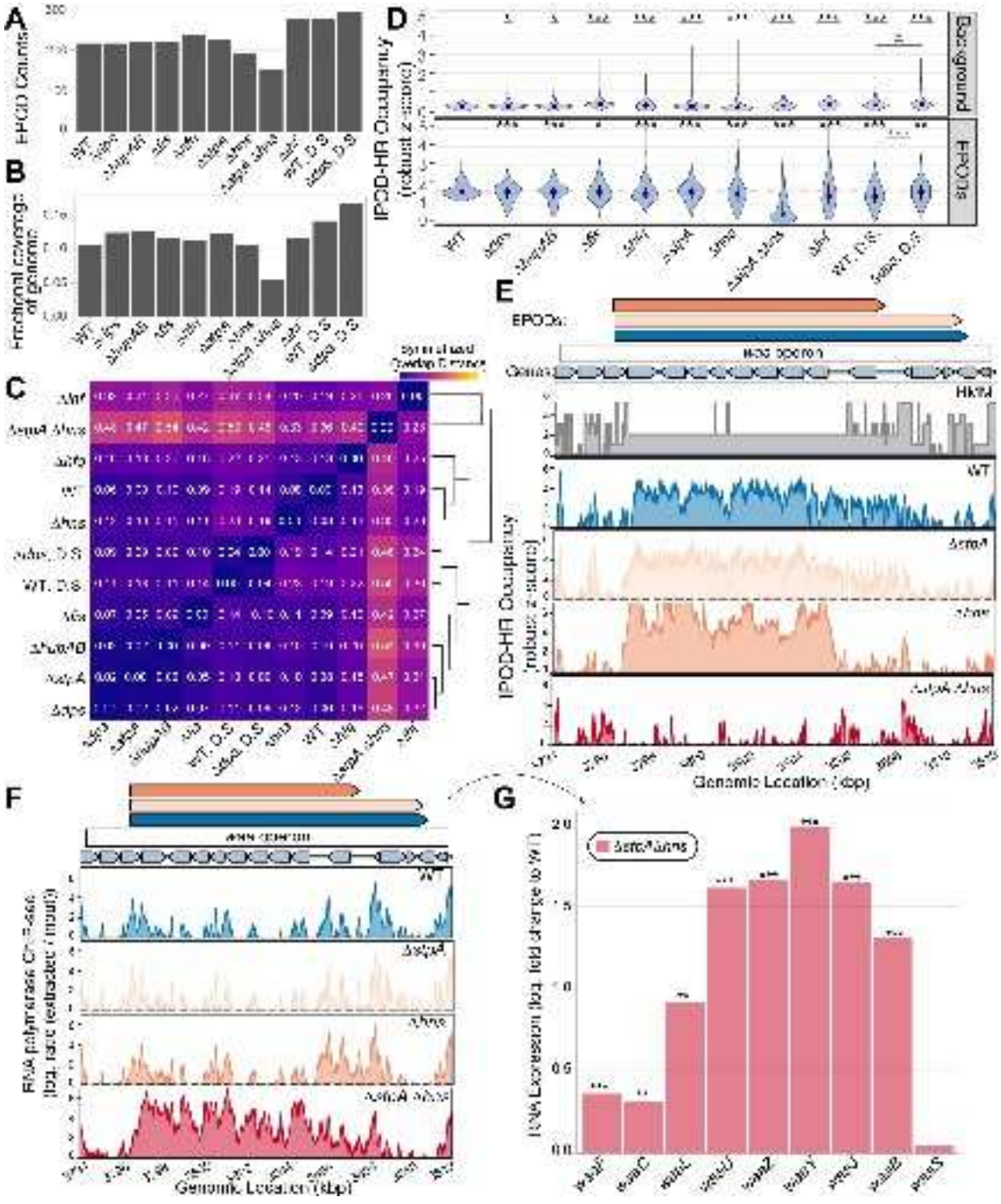

embj_2021108708_f2.tif

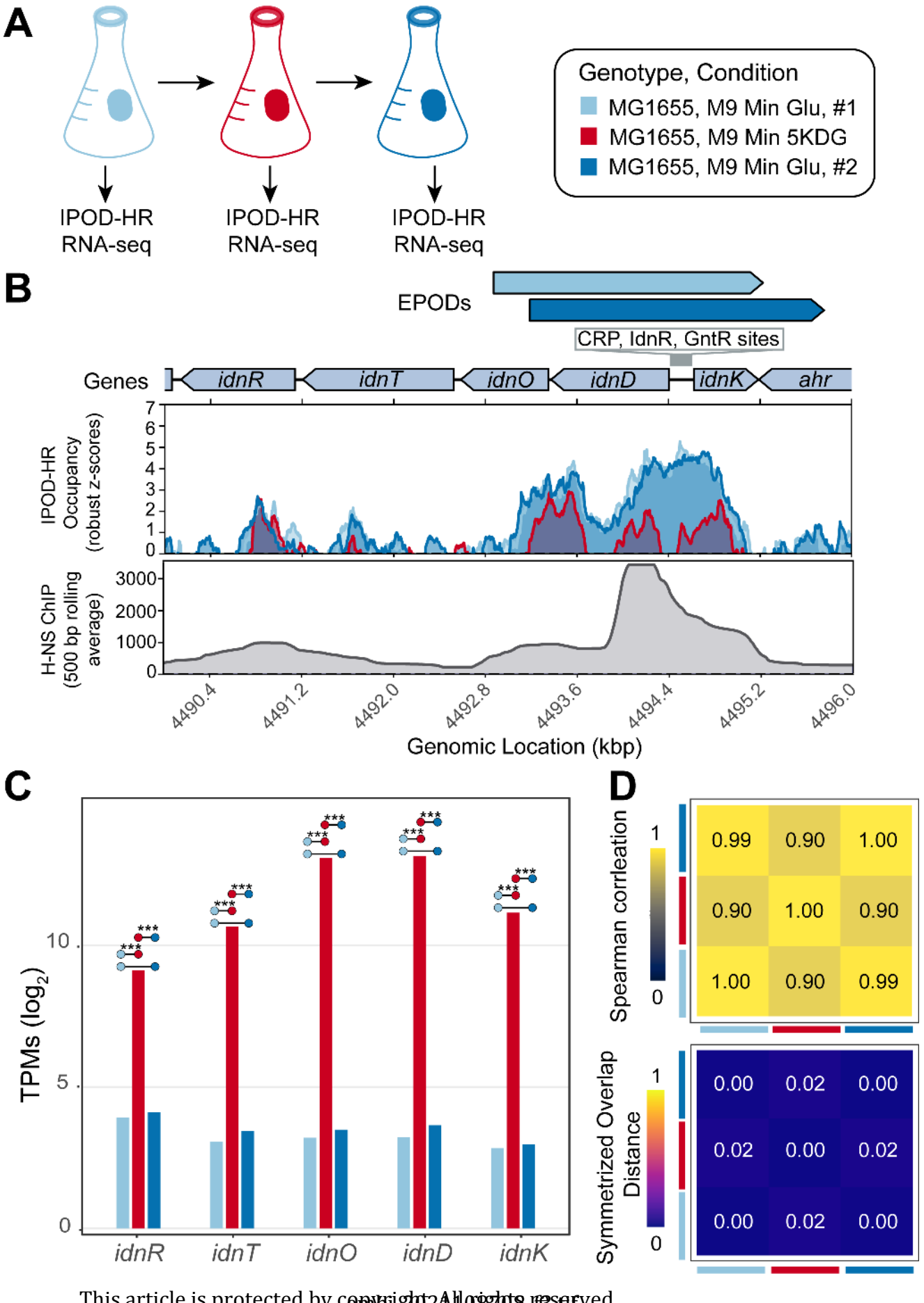

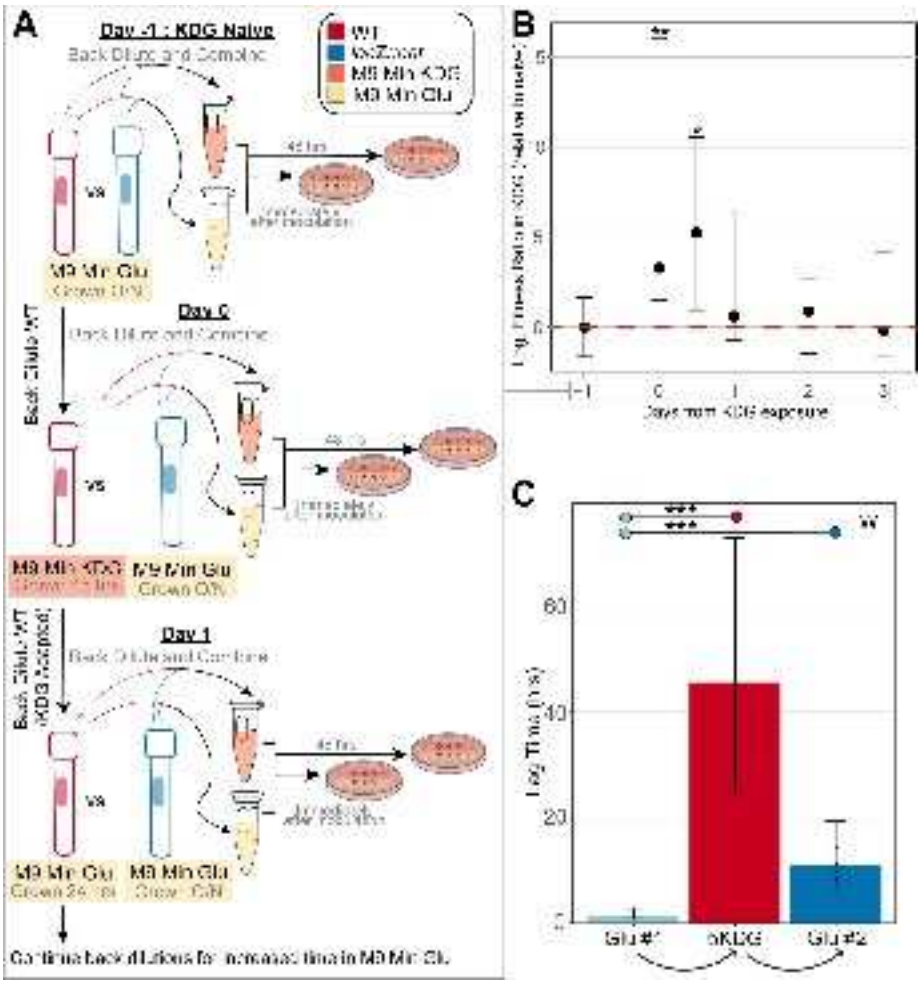

embj_2021108708_f4.tif

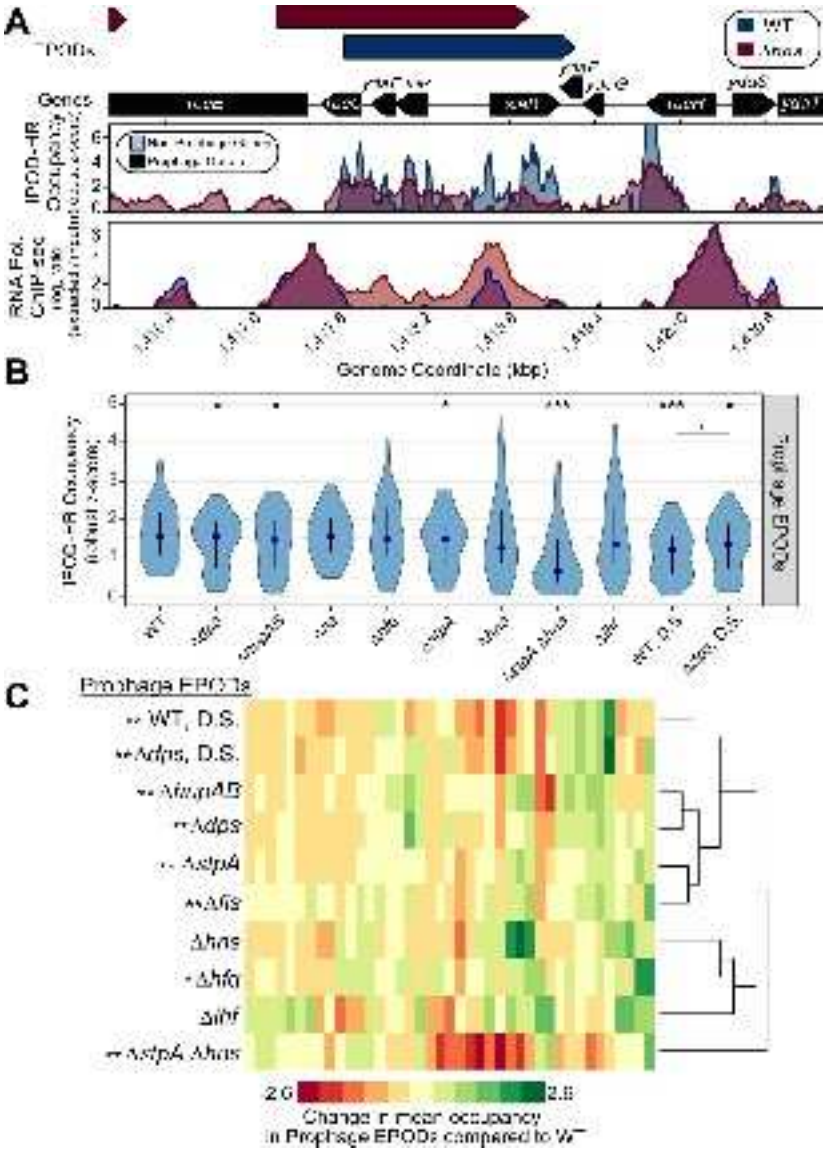

embj_2021108708_f5.tif

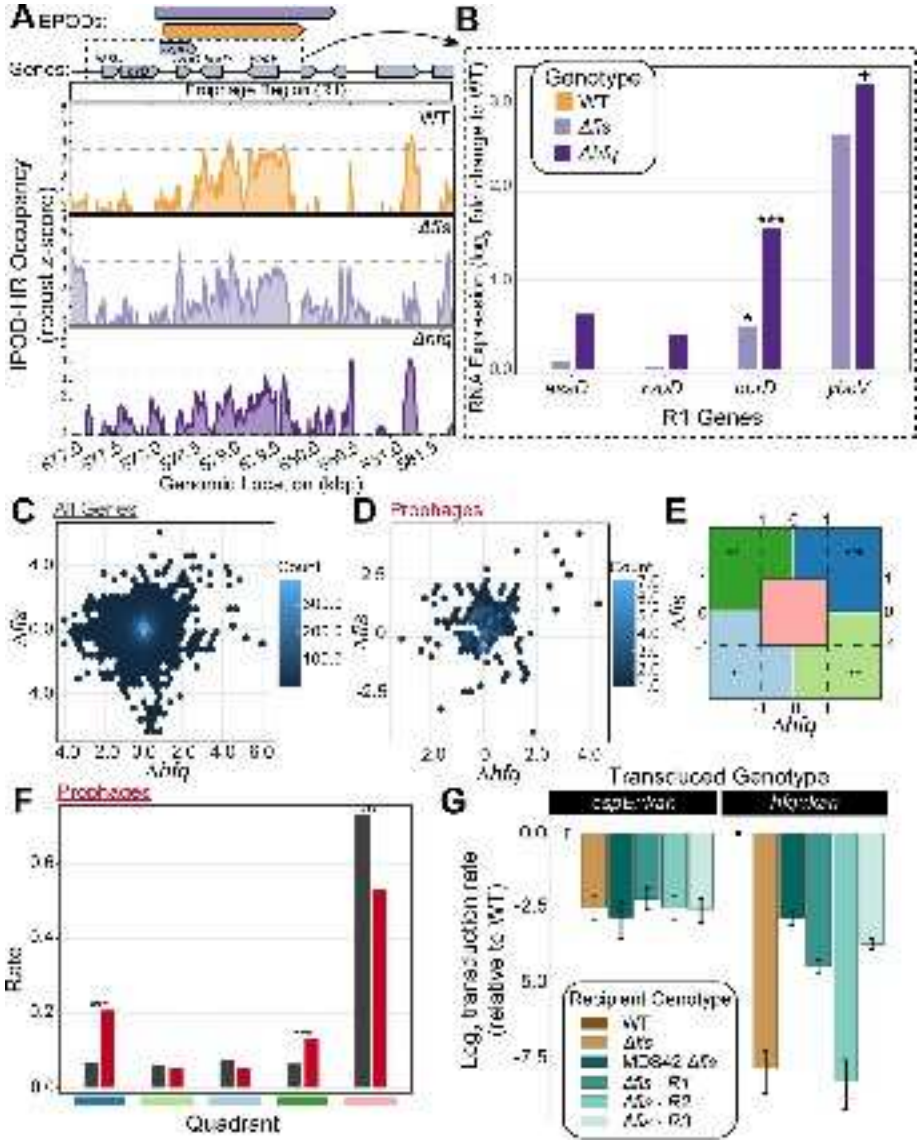

embj_2021108708_f6.tif

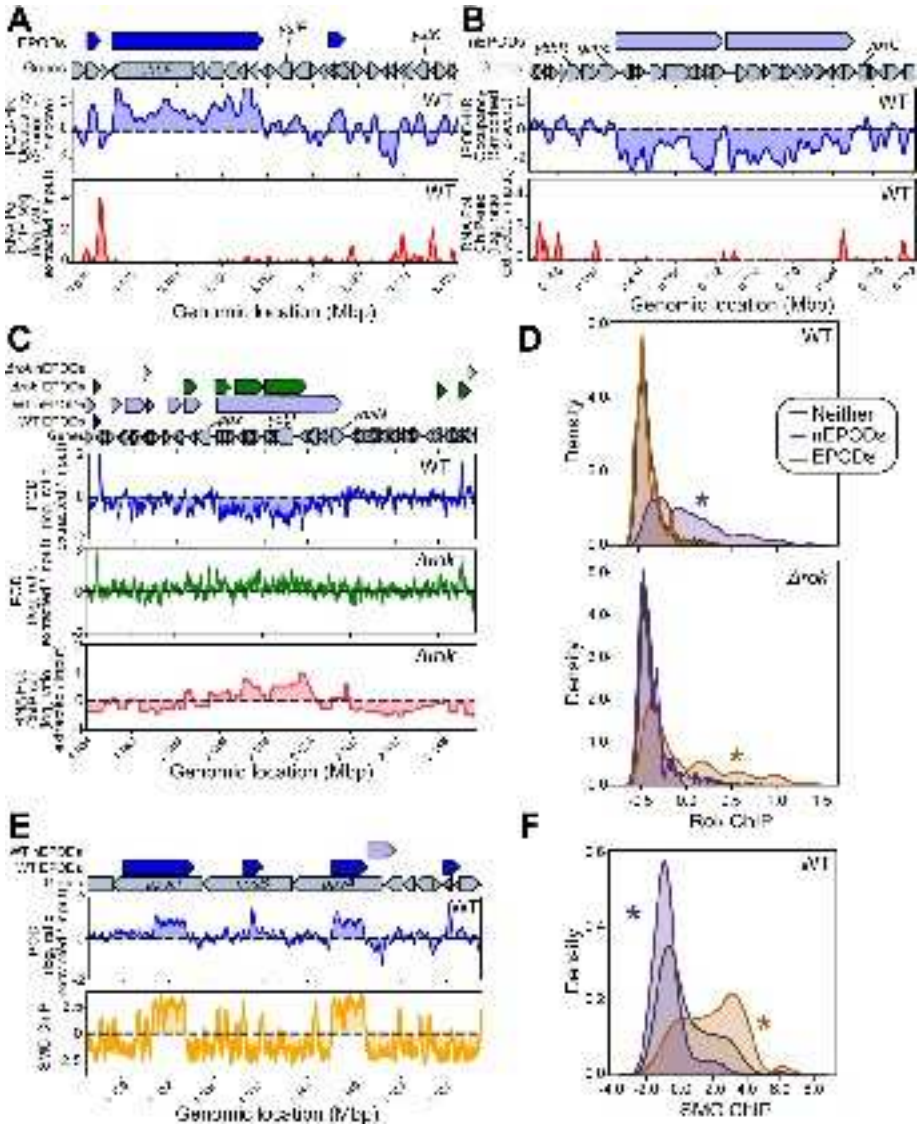

embj_2021108708_f7.tif